Sapphire Based Fiber-Optic Sensing for Extreme High Temperatures

Guo Yu

Thesis submitted to the Faculty of
the Virginia Polytechnic Institute and State University
in partial fulfillment of the requirements for the degree of

Master of Science
in
Electrical Engineering

Anbo Wang (Committee chair)
Gary Pickrell (Committee member)
Yong Xu (Committee member)

May 3rd, 2011
Blacksburg, Virginia

Keywords: Sapphire fiber, sensing, high temperature, harsh environment, EFPI, miniaturized, wafer sensor

Sapphire Based Fiber-Optic Sensing for Extreme High Temperatures

Guo Yu

Abstract

Temperature sensing is one of the most common and needed sensing technique, especially in harsh environment like a coal gasifier or an airplane engine. Single crystal sapphire has been studied in the last two decades as a candidate for harsh environment sensing task, due to its excellent mechanical and optical properties under extreme high temperature (over $1000℃$).

In this research, a sapphire wafer based Fabry-Perot (FP) interferometer sensor has been proposed, whose functional temperature measurement can go beyond $1600℃$. The size of the sensors can be limited to a $2cm$-length tube, with $2mm$ outer diameter, which is suitable for a wide range of harsh environment applications. The sensors have shown linear sensing response during $20\sim1200℃$ temperature calibration, with high sensitivity and resolution, and strong robustness, which are ready for the field test in real-world harsh environment.

Acknowledgement

The passing period of my research and thesis writing appears like a long but wonderful journey to me. I would like to give my greatest thanks to my advisor, Dr. Anbo Wang, who offered me the opportunity to pursue my Master's degree in Center for Photonics Technology, with such an amazing team and such exciting projects. This entire work would not be possible without the constant support and encouragement from him, who provided us not only inspiration and advice for the research and project, but also guidance and experiences from which my future career could be benefited. I would also thank Dr. Gary Pickrell and Dr. Yong Xu for their enormous help and suggestions for my research and thesis.

Special thanks to Dr. Evan Lally and Cheng Ma, as project managers as well as honest friends, for their generous assistance into every detail aspect of the research, and great personality which influenced our friendship and my daily experience. Particular gratitude goes to Georgi Ivanov, as co-worker and valuable partner, who repetitively inspires me in the research and shared tremendous thoughtful ideas with me in the past years. I would also thank my colleagues and dearest friends, Bo Dong, Dr. Gong, Zhipeng Tian, Kathy Wang, Tyler Shillig and Michael Fraser for the delightful time we have spent together.

Last but not least, huge appreciation goes to our sponsors, the U.S. Department of Energy, for their financial support on this challenging but exciting sapphire high temperature sensing project.

Table of Contents

Chapter 1. ***Introduction*** 1
1.1 Fiber optic sensing 1
1.2 Temperature sensor 2
1.3 Organization of Thesis 3
Chapter 2. ***Challenge of High Temperature Sensing and the Methodology of Sensor Design*** 4
2.1 Challenge of Temperature Sensing in Coal Gasifier 4
2.2 Choice of Sensor Material 5
2.3 Fabry-Perot Interferometer 7
2.4 Sensor Design 11
2.5 Interrogation System and Fringe Visibility 15
Chapter 3. ***Sensor Head Fabrication*** 19
3.1 Fabrication of Sapphire Wafer 19
3.2 Sensor Head Assembly 27
3.3 Sensor Head Evaluation 32
Chapter 4. ***Sensor Link Assembly and Signal Processing*** 34
4.1 Experimental Measurement of Loss in Sapphire Fiber 34
4.2 Silica-to-Sapphire Fiber Splicing 37
4.3 Sensor Link Assembly 44
4.4 Signal Processing and Temperature Calibration 47
Chapter 5. ***Conclusions*** 50
5.1 Conclusions 50
5.2 Suggestions for Future Work 51
Reference 53

List of Figures

Figure 2.2-1 Physical Properties of Sapphire 6
Figure 2.3-1 Structure of Fabry-Perot Interferometer 7
Figure 2.3-2 Typical Spectrum of Fabry-Perot Interferometer 8
Figure 2.3-3 Construction of an EFPI Sensor 9
Figure 2.3-4 Construction of an IFPI Sensor 9
Figure 2.3-5 Schematic of EFPI[22] 10
Figure 2.3-6 Fringe Visibility versus Cavity Length 11
Figure 2.4-1 Wafer-based Sapphire EFPI Sensor[17] 11
Figure 2.4-2 Sensor Head, Basic Structure and Dimensions 12
Figure 2.4-3 Silica to Sapphire fiber splicing 14
Figure 2.4-4 Sensor Link, Basic Structure and Dimensions 14
Figure 2.5-1 Schematic diagram of interrogation system 15
Figure 2.5-2 Spectrum and OPD calculation 16
Figure 2.5-3 Spectrum and fringe visibility 18
Figure 3.1-1 Ultrasonic cutter 20
Figure 3.1-2 Methods to improve ultrasonic cutting 21
Figure 3.1-3 Sapphire wafers cut by ultrasonic cutter 22
Figure 3.1-4 $1mm$ Sapphire disc under microscope 22
Figure 3.1-5 Dicing Wafer to Fit in the Inner Tubes 23
Figure 3.1-6 Wafer Dicing Process 24
Figure 3.1-7 Wafer Polishing 25
Figure 3.1-8 Experimental Result of Sapphire Wafer Polishing 25
Figure 3.1-9 Sapphire Wafers Fabricated 26
Figure 3.2-1 Sensor Assembly Setup 28
Figure 3.2-2 Laser Sealing Setup 29
Figure 3.2-3 Sealed Sensor Heads 30
Figure 3.3-1 Sensor Head Interrogation system 32
Figure 4.1-1 Experiment Setup for Loss Measurement in Sapphire Fiber 35
Figure 4.1-2 Spectrum Data for Loss Measurement 36
Figure 4.1-3 Curve Fitting Method for Loss Measurement 37
Figure 4.2-1 Silica-to-Sapphire Splicing 38
Figure 4.2-2 Comparison between Normal Splice with Angled Splice 40
Figure 4.2-3 Reflection Spectrum with $10°$ Angled Splicing 41
Figure 4.2-4 Reflection versus Angled Splicing Result 41
Figure 4.2-5 Configuration of Simulation for Fringe Visibility versus Reflection 42
Figure 4.2-6 Simulation of Fringe Visibility versus Reflection at Splicing Point 43
Figure 4.2-7 Fringe Visibility versus Angled Splicing Result 44
Figure 4.3-1 $10°$ Angled Polishing and Splicing 45
Figure 4.3-2 Sensor Link Assembly – detailed 45
Figure 4.3-3 Sensor Link Assembly Setup 46
Figure 4.4-1 Sensor 2 calibration Result – Run 1 49
Figure 4.4-2 Sensor 2 calibration Result – Run 2 49

Figure 5.1-1 Sensor Dimensions 50
Figure 5.2-1 Thin Film Anti-reflection Coating for Splicing Point 52

List of Tables

Table 3.1-1 Test results of ultrasonic cutter 21
Table 3.1-2 Comparison of Sapphire Wafer Fabrication Procedure 26
Table 3.2-1 Adhesive Curing Procedures 29
Table 3.2-2 Loss Analysis of Sensor head Assembly 31
Table 3.3-1 Fringe Visibility during Sensor Head Fabrication[1] 33
Table 4.2-1 Splicing Parameters for Silica-to-Sapphire Splicing (Sumitomo Type36) 38
Table 4.2-2 Fringe Visibility versus Angled Splicing Result 43

Chapter 1.

Introduction

When we talk about sensing, sensing of temperature is one of the oldest in history and most common. From daily weather report to air conditioners, temperature sensing lays under every aspect of our life, work and research. Different techniques of temperature sensing hold different sensitive ranges for various purposes. Mercury thermometers based on the thermal expansion and contraction nature are widely used to measure human body temperature. Electrical thermocouples based on the thermoelectric effect can serve most of industrial needs. Optical fiber, which first emerged in the 1960s[1], can also be fabricated into temperature sensors, with its own advantage and properties.

1.1 Fiber optic sensing

The field of fiber optic sensing started to bloom soon after the invention of optical fiber. In 1977, A. J. Rogers demonstrated an optical method to measure voltage and current using optical fiber[2]. And after decades of rapid development, fiber optic sensing has now been adapted into a method of largely diversified measurement. Besides temperature, it can also be used to sense strain, pressure[3], gas concentration[4], fluid flows, etc. Fiber optic sensing has already presented advantages over conventional sensing approaches in several areas[5]. Such advantages are embodied, but not limited, in small size, light weight, immunity to electromagnetic (EM) interference, electrical passivity, potential for dense multiplexing, high resolution and large dynamic range. Especially, for some harsh environment such as high temperature and strong EM field, where conventional methods can not apply, fiber optic sensing provides an alternative approach and so far has gotten great

development.

1.2 Temperature sensor

Temperature sensing with the aid of optical fiber rose soon after the first fiber optic sensing was realized. In 1980, William Quick et al, invented a fiber optic temperature sensor based on the amplitude decay rate and wavelength sensitivity to temperature[6]. And the sensible temperature bonds are also quickly broken. In 1991, Lee and Taylor demonstrated an Fabry-Perot temperature sensor which worked up to $600°C$[7]. Later in 1997, Zhang et al reported an intrinsic ND-doped fiber thermometer over the range from -196 to 750 °C[8]. Recently, the temperature measurement has been increased to over $1000°C$[9][10].

However, beyond $1000°C$, conventional silica-based fibers start to encounter problems like dopant diffusion and degradation in mechanical properties[11]. More attention has been drawn towards single crystal fiber due to their high mechanical performance and optical properties at extreme high temperature. Currently most semiconductor industries use radiation-based temperature sensors with single crystal sapphire fiber as the waveguide for monitoring rapid temperature change[12][13]. Other methods like fluorescence-based sensors also exist, which use doped fiber excited by pulsed laser to generate fluorescence, the decay time of which is related with temperature and used as calibration[14]. Among these methods, Fabry-Perot (FP) interferometric sensors have a relatively simple configuration while keep high accuracy and high resolution. Plentiful work has been done in this field, both in theory and practical demonstration. Wang et al proposed both intrinsic[15] and extrinsic[16] sapphire-based FP temperature sensors. This research seeks for a solution to improve the sapphire fiber based FP temperature sensor from the original design by Zhu[17]. The goal of this thesis is to prepare fully assembled sensors for a field test in coal gasifier.

1.3 Organization of Thesis

The rest chapters of the thesis are organized this way: In Chapter 2 the challenge of high temperature sensing will be outlined and the methodology of sensor design to overcome it. Chapter 3 presents the detail procedure to fabricate the sensor head, and Chapter 4 discusses the final assembly of the sensor link as well as the signal processing method for data interpretation. And finally, we will conclude in Chapter 5 and provide some scope for further research.

Chapter 2.

Challenge of High Temperature Sensing and the Methodology of Sensor Design

In the previous chapter, we introduced the research on fiber-optical sensing using single crystal fiber for temperature sensors which can go beyond 1000℃. In this chapter, we will specify the needs to the project of ultra-high temperature sensing for coal gasifier. The challenge of such harsh environment will be explained in detail in Section 2.1, followed by the discussion of choice of materials for the sensor fabrication in Section 2.2. In Section 2.3 we will briefly review the theory of Fabry-Perot interferometer, which is the fundamental methodology of our sensor design. The final design of whole sensor link will be presented in Section 2.4, and the interrogation system for the sensor will be discussed in Section 2.5.

2.1 Challenge of Temperature Sensing in Coal Gasifier

Coal gasification is one of the most versatile and clean ways to convert coal into electricity, hydrogen and other valuable energy products. Coal gasification is able to remove up to 99% of pollutant forming impurities, and is more efficient than conventional coal-fired boilers. During the coal gasification process, real-time temperature measurements are needed for reliability and efficiency, also very important for process control in the coal fired power plants.

In a coal gasifier, instead of burned, coal goes through a thermo-chemical process by high temperature and pressure in an oxygen-limited environment. It will chemically break down into basic chemical constituents, such as carbon monoxide (CO) and hydrogen (H_2) [18][19]. Refractory liners are used in the entrained-flow slagging gasifiers to protect the gasifier shell from the severe environment, including extremely high

temperatures (1250-1550°C), large temperature gradient, rapid temperature changes, high pressure (400psi and up), corrosive gases, particulate erosion and molten slag attack.

Reliability and accuracy of temperature measurement is a major concern for safe and efficient gasifier operation. Too high a temperature will reduce the conversion efficiency and significantly shorten the lifetime of refractory liners, which is a critical factor limiting the system availability. While too low a temperature will cause the molten slag become viscous, blocking the gases flowing in and out the gasifier. Currently used thermocouples for coal gasifier can only function about 30-45 days. And the replacement is costly for both money and time.

2.2 Choice of Sensor Material

Facing such harsh environment, the choice of material for sensor design becomes extremely crucial, because in most circumstance, the performance and limits of a fiber-optical sensor are determined by the material of which the sensor is made.

The first criterion for the choice of material is obvious, that the material of both the sensor and the fiber need to be able to survive at the ultra-high temperature within the gasifier (1250-1550 °C), and maintain relative good optical performance and mechanical properties. These requirements would rule out a large percent of our choices, like commonly used fused silica, most kinds of the doped silica fiber (very few types of doped silica fiber can survive at the temperature we needed[8]), silicon carbide (SiC) and polymers.

The second criterion for the choice of materials is based on the concern of material consistency. Due to the high temperature, severe temperature gradient and rapid change, even small difference in thermal expansion coefficient would result in breakage, causing great compromise of sensors' performance. Therefore, fabricating the sensor with uniform materials would be more reliable, and the sensor would have better chance to survive the harsh environment of coal gasifier.

Single crystal fibers like sapphire (single crystal alumina, Al_2O_3) fiber and single crystal zirconia (ZrO_2) fiber are perfect candidates for the above requirements. And among these fibers, sapphire fiber has been used in the majority of the proposed fiber-optical sensors for high temperature. Figure 2.2-1 shows the crystal structure and the thermal expansion as well as the transparency versus light in different wavelength.

Additionally, with sapphire fiber, we can use sapphire wafer as the sensing component, and alumina tubes as protection assembly, which guarantee the uniform of materials of sensor and the cost efficiency. Detail explanation of the combination of sensing components, sapphire fiber and protection components will be discussed in the Section 2.4.

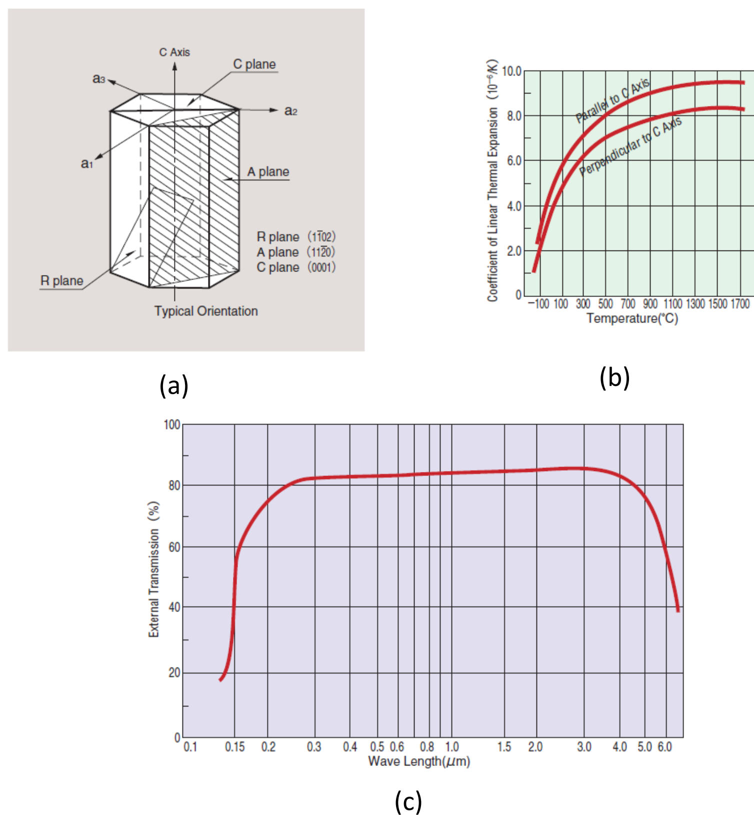

Figure 2.2-1 Physical Properties of Sapphire

(a), the unit cell of sapphire crystal, (b), the thermal expansion coefficient of sapphire in different direction (c), the transmission curve of light with 1mm sapphire wafer

2.3 Fabry-Perot Interferometer

In the last several decades, fiber optic sensing has been developed into diverse technologies, which have provided large amount of competitive applications compared with conventional sensing methods. There are several main categories of fiber-optical sensing technique, including fiber gratings (Fiber Bragg Grating, Long Period Grating, etc.), interferometers (Fabry-Perot interferometer, Michelson interferometer, etc.), fluorescence-based sensing, Raman scattering, and so on. Fabry-Perot interferometer inherits the advantage of simple structure and configuration, high resolution and large dynamic range, which is an ideal fit for our ultra-high temperature sensing project.

2.3.1 Mechanism of Fabry-Perot Interferometer

A Fabry-Perot (FP) interferometer is typically made of a transparent plate (also known as FP cavity) with two reflecting surfaces, or two highly parallelized reflecting mirrors. Figure 2.3-1 demonstrates a basic structure of FP interferometer, where the length of the FP cavity is l and the refractive index is n, R_1 and R_2 represent the reflected light intensity from the two surfaces of the FP cavity, assuming a plane wave of monochromatic incident light.

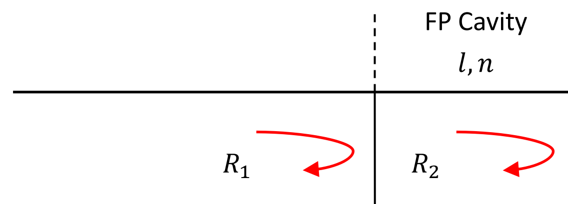

Figure 2.3-1 Structure of Fabry-Perot Interferometer

Multiple reflections from the two surfaces will generate an interference pattern. If R_1 and R_2 are far less than unity, higher order reflections can be neglected, and the total reflection would be approximately the superposition of R_1 and R_2, where ϕ_0 is the

initial phase shift.

$$R_{total} = R_1 + R_2 - 2\sqrt{R_1 R_2}\cos\left(2\pi \times \frac{2nl}{\lambda} + \phi_0\right) \quad (2\text{-}1)$$

In practice, the light we used has a non-zero bandwidth, thus the reflected light would result a spectrum, collected by a spectrometer with corresponding bandwidth. Figure 2.3-2 is a typical spectrum from an FP interferometer, where each data point in Figure 2.3-2 obeys the principle of Equation 2-1. The overall spectrum data can be used to calculate the optical path distance (OPD), which is $2nl$ in Equation 2-1. The changes in OPD are able to characterize a lot of physical parameters, like temperature (materials with temperature dependent refraction index), strain (changes in cavity length) and so on. By calibrating the change of OPD with the parameter intended to measure, the sensing is realized.

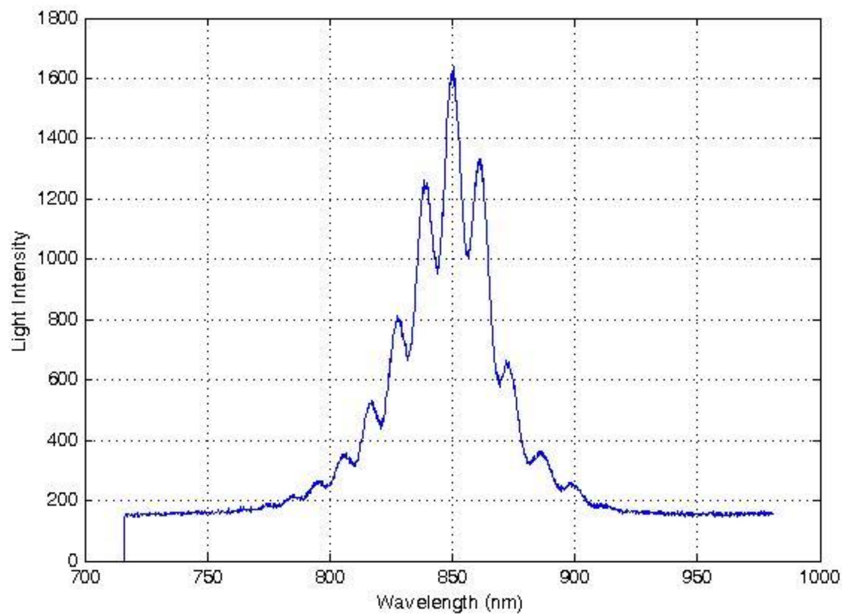

Figure 2.3-2 Typical Spectrum of Fabry-Perot Interferometer

2.3.2 IFPI and EFPI Sensors

Based on different structures of the FP cavity, FP sensors are usually classified into extrinsic Fabry-Perot interferometer (EFPI) sensors or intrinsic Fabry-Perot interferometer (IFPI) sensors. The FP cavity of EFPI sensors are outside of the fiber (Figure 2.3-3), the air gap between two well cleaved fiber forms the FP cavity, and the

reflections from two fiber ends cause the interference. While the FP cavity of IFPI sensors is made within the fiber (or fiber itself), as shown in Figure 2.3-4, the FP cavity is defined by the small section of multi-mode fiber, and the interference pattern is produced by two reflections at splicing points.

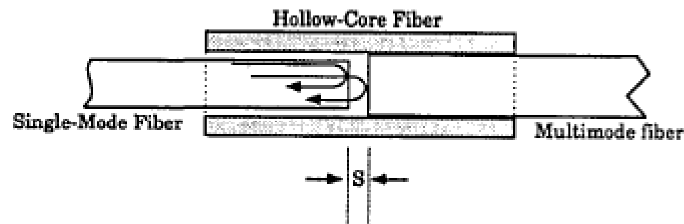

Figure 2.3-3 Construction of an EFPI Sensor[20]

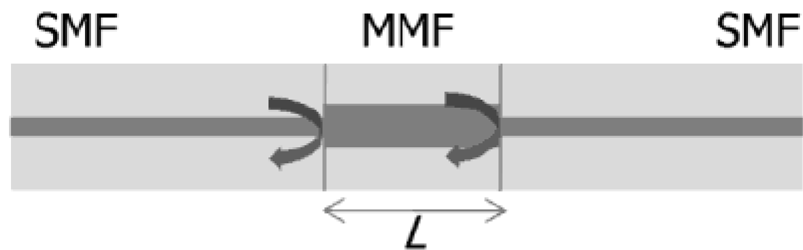

Figure 2.3-4 Construction of an IFPI Sensor[21]

2.3.3 Sapphire Wafer Based EFPI Sensor

Cheng et al recently developed a new model to describe EFPI sensors, both for single mode fibers and multimode fibers[22]. Although the sapphire fiber used in this research is not ordinary silica-based multimode fiber, Cheng's analysis can still be adopted as theoretical guidance for the sensor fabrication.

As shown in Figure 2.3-5, the reflected light from the second surface of the FP cavity can be equivalent with propagating light into a mirror fiber. Here E_1 and E_2 denote the electric field distribution at first and second reflection surfaces, and Δ refers to the OPD of the FP cavity.

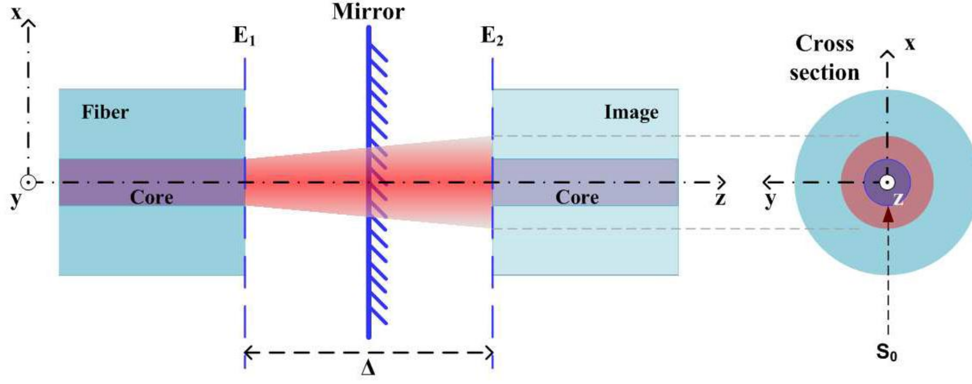

Figure 2.3-5 Schematic of EFPI[22]

Then the detected light intensity is the sum of the two electric fields over the area of fiber core S_0.

$$P = \iint_{S_0} (E_1 + E_2)^*(E_1 + E_2)\mathrm{ds} \tag{2-2}$$

And can be expressed as a function of the OPD

$$P(\Delta) = (1+\nu)P_1 - 2\int_0^k I(k_z)\cos\big((k_z - k)\Delta + k\Delta\big)\, k_z \mathrm{dk_z} \tag{2-3}$$

where $P_1 = \iint_{S_0} E_1 E_1^* \mathrm{ds}$ and $\nu P_1 = \iint_{S_0} E_2 E_2^* \mathrm{ds}$, and $I(k_z)$ is the optical power density distribution along the z axis in the FP cavity and k_z is the wavenumber domain z direction.

Although analytical expression of $I(k_z)$ is very difficult to obtain if multimode fiber is used, due to the large modal volume of propagating light. However, the intensity distribution is equivalent to measure the output angular distribution of light intensity, which can be easily calculated from experimental data.

Figure 2.3-6 shows the trends of both theoretical and experimental results, where the fringe visibility is a value to quantitatively scale the spectrum quality of EFPI sensors. Further explanation of fringe visibility will be presented in the following sections. Figure 2.3-6 indicates that in order to achieve high quality sensors, reducing the OPD of FP cavity, or thinning the sapphire wafer is necessary, and below the thickness of $30\mu m$ (which corresponding to $\approx 50\mu m$ cavity length in air), the fringe visibility could increase dramatically.

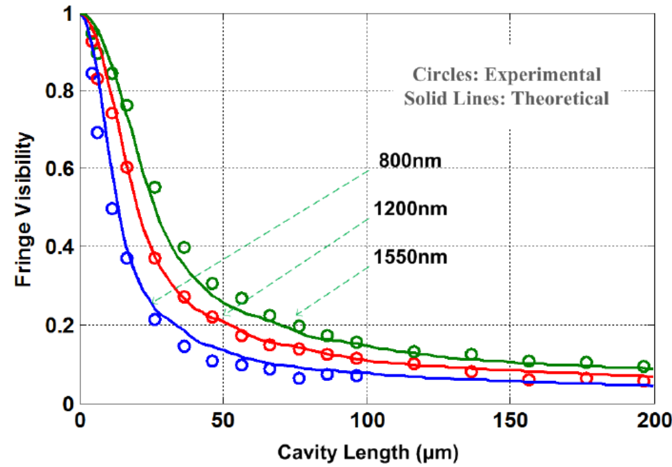

Figure 2.3-6 Fringe Visibility versus Cavity Length[22]

Based on silica MMF with core diameter $105\mu m$, numerical aperture 0.22, FP cavity is air

2.4 Sensor Design

As we discussed in the previous sections, sapphire fiber will be applied at the ultra-high temperature region, i.e. we will use sapphire fiber with $75\mu m$ diameter, which is commercially available. Considering the difficulty to fabricate an FP cavity within sapphire fiber, a sapphire wafer is chosen as the sensing component, which will form an EFPI sensor (as shown in Figure 2.4-1).

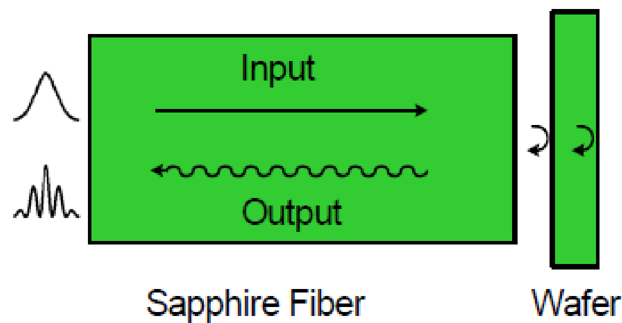

Figure 2.4-1 Wafer-based Sapphire EFPI Sensor[17]

In order to guarantee the uniformity of materials, both the sapphire fiber and wafer are cut in C-plane, since the physical properties of different planes of sapphire crystal are not identical, as shown in Figure 2.2-1. For stable attachment of the sapphire fiber

with sapphire wafer, we designed a sensor head structure (Figure 2.4-2), within which the sapphire wafer is immersed in a single-end-sealed alumina tube. The sapphire fiber can see the wafer perpendicularly by inserting the fiber through the open end of the sensor head. Additionally, the sealed sensor head can also protect the sapphire wafer from harsh environment in the gasifier. Detailed procedure to manufacture the sensor head will be presented in the next chapter.

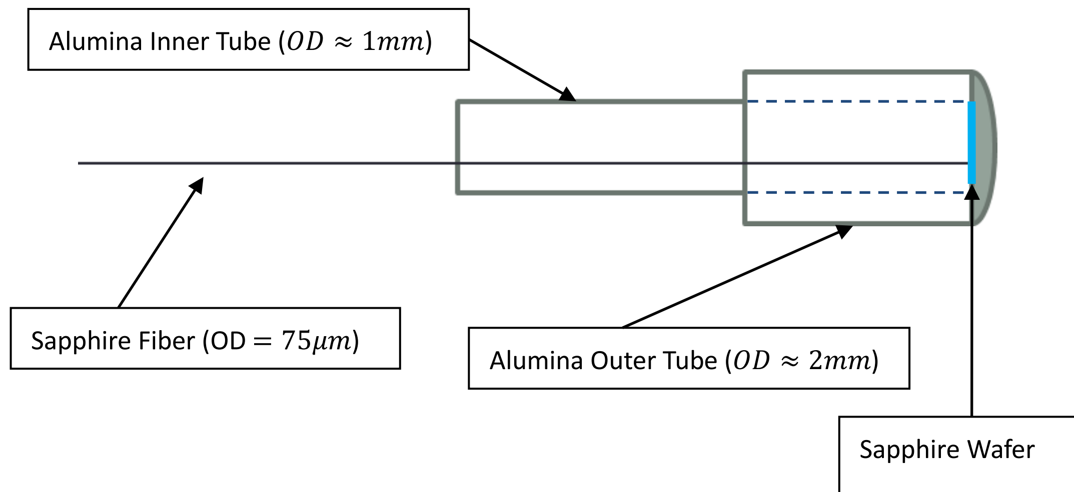

Figure 2.4-2 Sensor Head, Basic Structure and Dimensions

2.4.1 Remaining Challenges

Although the optical and mechanical properties of sapphire material are qualified for the extreme harsh environment of coal gasifier, there are still some difficulties remain, which prevent the direct use of sapphire fiber for temperature sensing:

- Weakened interference signal

Since sapphire fiber is grown in form of single crystal, it does not have a cladding like normal silica multimode fiber. Therefore sapphire fiber of large diameter has greater numerical aperture (NA) and is highly multimoded. For highly multimoded fiber, the surface quality and parallelism of two reflection surfaces in an EFPI sensor are extreme important for high quality interference signal[23], even a small wedge angle could result critical decrease in interference signal strength[24].

- Sapphire fiber loss

Unlike the normal silica fiber with cladding, sapphire fiber is a bare fiber without any cladding or coating. Also considering sapphire fiber as a highly multimoded fiber, the light signal has a greater chance to be scattered off the fiber, causing greater loss in sapphire fiber than other conventional fiber. Such loss not only limits the length of sapphire fiber that can be used in the sensor link, but also raises a great challenge for the signal acquisition and signal processing. Detailed experiments regarding the loss of sapphire fiber will be presented in Chapter 4.

- Difficulty in interrogation

Currently, there is no fiber-optical interrogation system able to adapt sapphire fiber directly. It is necessary to connect the sapphire fiber to commonly used silica-fiber-based systems. For free space interrogation, objective lenses are used to guide the light signal in and out of sapphire fiber. However, in our fiber based sensor link, we need to splice the sapphire fiber to a silica fiber. According to the extreme high melting temperature of sapphire (over 2000℃), conventional fusing splicers can not melt sapphire fiber as it does in the normal silica-to-silica splice. Instead, silica fiber with low softening temperature core is used[17], as shown in Figure 2.4-3. During the splicing, the large core of silica fiber is softened, and the sapphire fiber is inserted into the core of silica fiber.

Such splicing point would result bigger loss than a normal silica-to-silica splice. Improving the quality of the splicing point becomes a critical step of the sensor link design, especially with the weakened interference pattern and great loss in sapphire fiber. Angled polishing and splicing techniques are applied to reduce the loss especially the reflection at the splicing point, which will be further explained in Chapter 4.

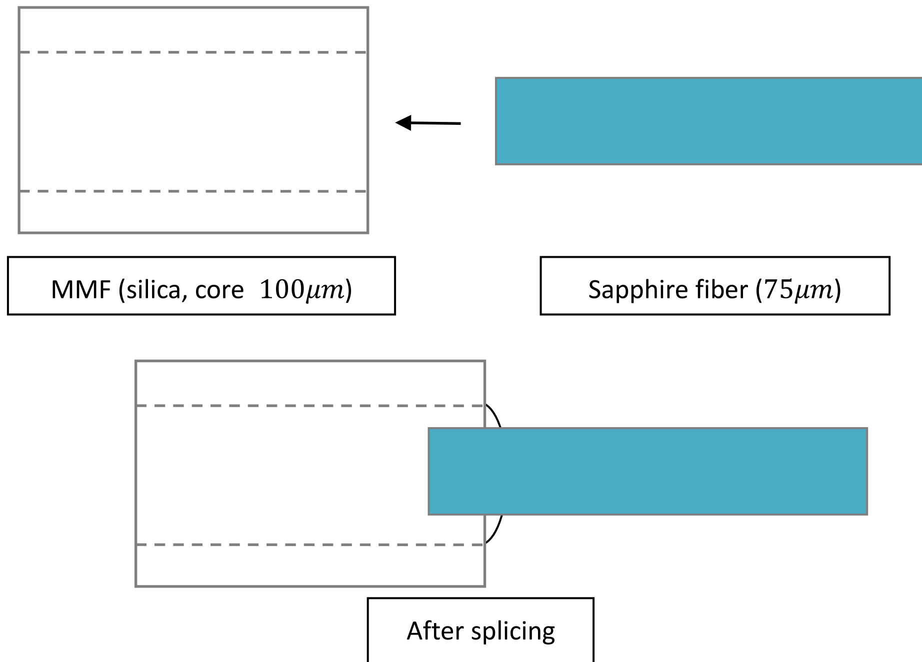

Figure 2.4-3 Silica to Sapphire fiber splicing

2.4.2 Sensor Link

Including all the concerns above, and taking into account the dimension and temperature distribution within the sensing field, we designed the whole sensor link shown in Figure 2.4-4:

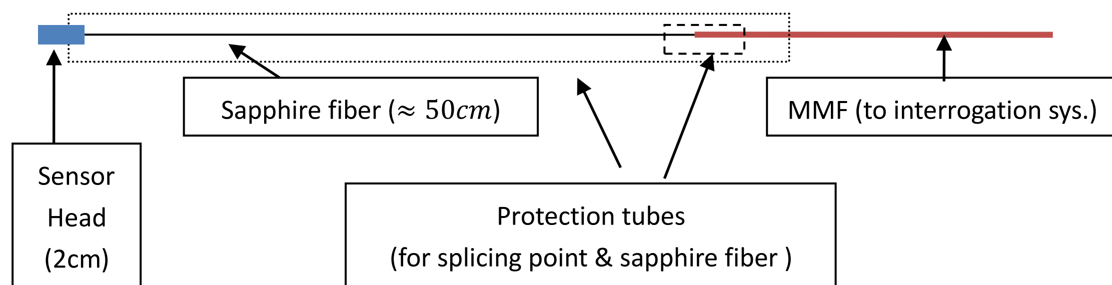

Figure 2.4-4 Sensor Link, Basic Structure and Dimensions

The length of sapphire fiber is chosen to be around $50cm$, according to the temperature gradient in the sensing area, so that the temperature at the sapphire-to-silica splicing point will not exceed 500°C. Additional protection tubes

will be added along the sensor link, preventing sapphire fiber or splicing point from breaking. The materials used for protection tubes are alumina/sapphire for high temperature region (above 1000℃), and silica for relative low temperature region (below 500℃). Such choice of material is also for the consideration of material uniformity.

2.5 Interrogation System and Fringe Visibility

The interrogation system we used is a conventional white light based spectrum analysis system, as demonstrated in Figure 2.5-1. It contains an OceanOptics spectrometer (OceanOptics USB2000[25]), the detectable wavelength range of which is $200{\sim}1100nm$, an LED white light source centered around $850nm$, and a MMF coupler, to guide the light signal in and out from the sensor link.

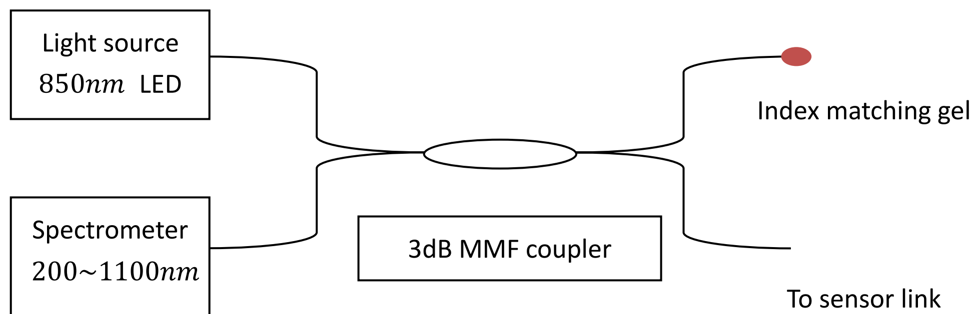

Figure 2.5-1 Schematic diagram of interrogation system

The light signal is first generated at the light source, which then goes through the coupler into the two arms on the right side. One arm of the MMF coupler is immersed in index match gel to eliminate the reflection from that arm, which, if remaining untreated, would raise the background of receiving signal level. While the other arm (the sensing arm) is connected to the sensor link, reflected by the sapphire wafer, forming an interference pattern. The reflected light again goes through the coupler, half of which is guided into the spectrometer. The spectrometer is connected with a computer through a USB port, from which the interference signal data can be

collected and displayed.

The total light signal received by the spectrometer can be described by Equation 2-4,

$$I_{total}(\lambda) = I_{DC}(\lambda) + I_s(\lambda)R_{splice} + A \times I_s(\lambda)(R_{end} + R_{total}) \quad (2\text{-}4)$$

where I_{DC} refers to the background signal from blackbody radiation and dark current of spectrometer. I_s refers to the light signal from the LED light source. R_{splice} is the reflection coefficient at the silica-to-sapphire splicing point. A represents the attenuation in the sapphire fiber. R_{end} is the reflection coefficient at the end of sapphire fiber. R_{total} is the real interference pattern, which equals to,

$$R_{total} = R_1 + R_2 + 2\sqrt{R_1R_2}\cos\left(2\pi \times \frac{2n(T)l(T)}{\lambda}\right) \quad (2\text{-}5)$$

R_1 and R_2 are reflection coefficients at the two surfaces of the sapphire wafer, $n(T)$ and $l(T)$ are the temperature dependent refractive index and thickness of sapphire wafer. Combine Equation 2-4 with Equation 2-5,

$$I_{total}(\lambda) = I'_{DC}(\lambda) + A \times \left(R_{DC}(\lambda) + R_{AC}(\lambda)\cos\left(\frac{2\pi \times OPD(T)}{\lambda}\right)\right) \quad (2\text{-}6)$$

Here we marked the slow-varying components with “DC”, $I'_{DC}(\lambda) = I_{DC}(\lambda) + I_s(\lambda)R_{splice}$ and $R_{DC}(\lambda) = I_s(\lambda)(R_{end} + R_1 + R_2)$. The cosine related components are marked as “AC”, $R_{AC}(\lambda) = 2I_s(\lambda)\sqrt{R_1R_2}$. And OPD is the optical path distance, $OPD = 2n(T)l(T)$, is temperature dependent and essential sensor mechanism.

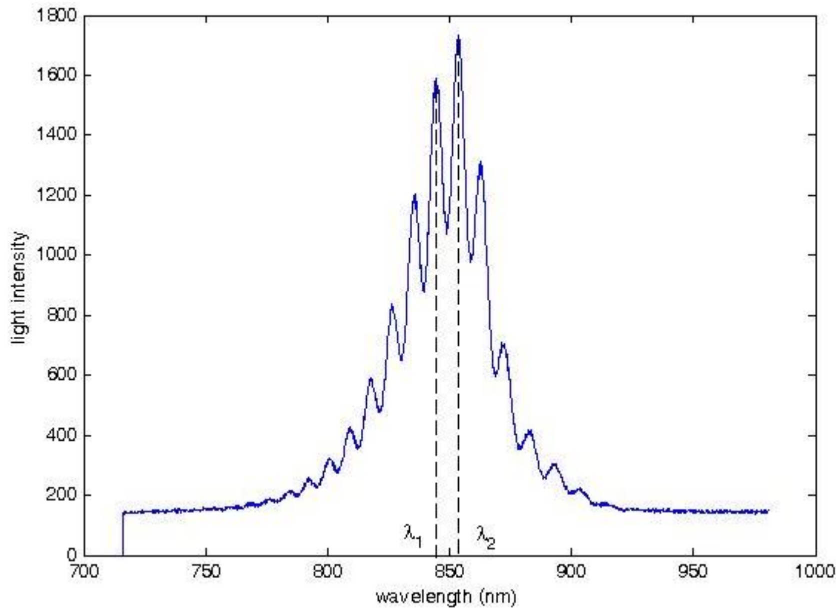

Figure 2.5-2 Spectrum and OPD calculation

Figure 2.5-2 is an example of spectrum we received from the sensor. A simple calculation directly comes from Equation 2-6, all the peak values in the spectrum indicate $\frac{OPD(T)}{\lambda} = n$, where n is an integer number. So for two adjacent peaks at λ_1 and λ_2 ($\lambda_2 > \lambda_1$), we have:

$$\begin{cases} OPD = \lambda_1(n+1) \\ OPD = \lambda_2 n \end{cases} => OPD = \frac{\lambda_1\lambda_2}{\lambda_2-\lambda_1} \tag{2-7}$$

Equation 2-7 gives the relationship between the interference signal and the OPD, which will be used as the calibration of temperature measurement. It is clear that the accuracy of λ_1 and λ_2 really define the resolution of the OPD, and the temperature. By differentiating the both sides of Equation 2-7, we have:

$$\Delta OPD = \Delta\left(\frac{\lambda_1\lambda_2}{\lambda_2-\lambda_1}\right) = \frac{\Delta(\lambda_1\lambda_2)(\lambda_2-\lambda_1) - \Delta(\lambda_2-\lambda_1)\lambda_1\lambda_2}{(\lambda_2-\lambda_1)^2}$$

$$= \frac{(\Delta\lambda_1\lambda_2 + \lambda_1\Delta\lambda_2)(\lambda_2-\lambda_1) - (\Delta\lambda_2-\Delta\lambda_1)\lambda_1\lambda_2}{(\lambda_2-\lambda_1)^2} = \frac{\Delta\lambda_1\lambda_2^2 - \Delta\lambda_2\lambda_1^2}{(\lambda_2-\lambda_1)^2}$$

Therefore,

$$\frac{\Delta OPD}{OPD} = \frac{\frac{\Delta\lambda_1}{\lambda_1}\lambda_2 - \frac{\Delta\lambda_2}{\lambda_2}\lambda_1}{\lambda_2-\lambda_1} \tag{2-8}$$

Since λ_1, λ_2 are any adjacent peaks on the spectrum, it is reasonable to assume $\Delta\lambda_1$ and $\Delta\lambda_2$ are iid (independent identical distribution), represented by $\Delta\lambda$. Then Equation 2-8 can be simplified,

$$\frac{\Delta OPD}{OPD} = \frac{\lambda_1+\lambda_2}{\lambda_2-\lambda_1}\Delta\lambda \tag{2-9}$$

In order to improve the resolution, we used some signal processing methods such as centroid algorithm and parabolic curve fitting to determine the peak positions (λ_n). Further discussion of the signal processing will be presented in Chapter 4.

In order to evaluate the quality of a sensor link through the spectrum, we can treat the spectrum as a combination of a slow-varying background and a rapid-varying cosine-shaped interference pattern, as shown in Figure 2.5-3. The latter part is related to the OPD. The fringe visibility is defined by the ratio of the rapid-varying interference signal and the slow-varying background components,

$$FV = \frac{I_{max} - I_{min}}{I_{max} + I_{min}} \tag{2-10}$$

where I_{max} and I_{min} are the maximum and minimum light intensities of a local range of wavelength, i.e. the adjacent peak and valley value. The fringe visibility of whole spectrum can be calculated by averaging several peaks and valleys. It would directly show the percentage of the interference signal from the total light signal received, which is the measurement of sensor link quality.

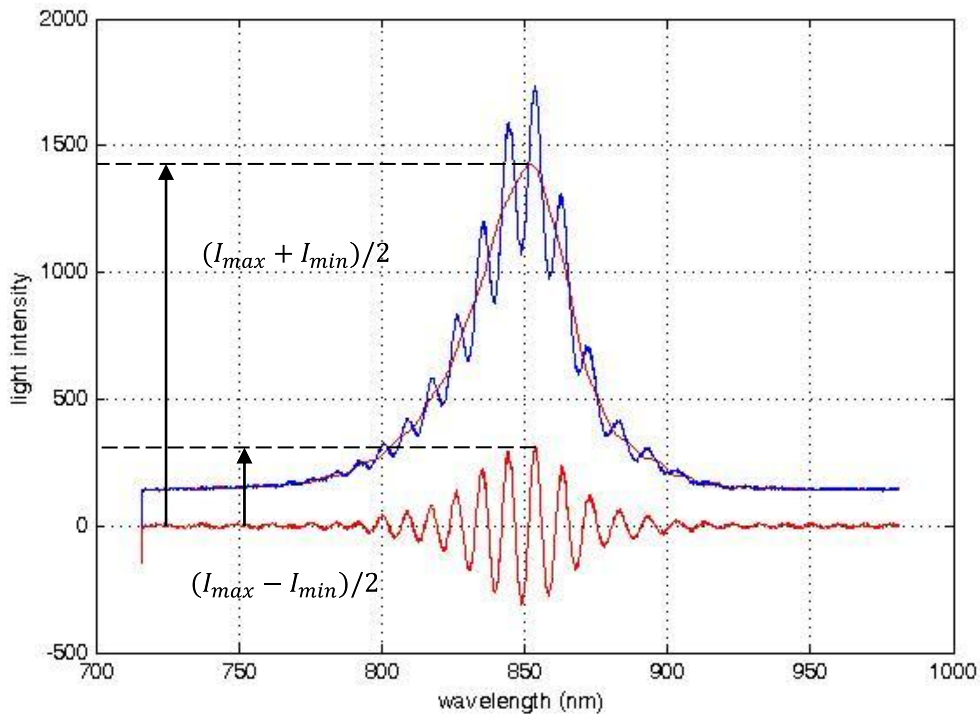

Figure 2.5-3 Spectrum and fringe visibility
Two red curves represent the background and the interference pattern, add them together will get the original spectrum

Chapter 3.

Sensor Head Fabrication

As we described in the previous chapter, the sensing components of our high temperature sensor are sapphire wafers immersed in single ended alumina tubes. Such structures are referred as sensor heads.

Among the components of the whole high temperature sensing system, the sensor head is the most important part. Since the quality of the sapphire wafer mostly determines the fringe visibility of the sensor. So far, we have been able to achieve fringe visibility over 0.5 with $20\mu m$ thickness sapphire wafers, interrogated through normal multimode silica fiber. After the sensor fabrication, we can still preserve fringe visibility over 0.2, interrogated by $50cm$ sapphire fiber.

The rest of the chapter will be organized as follows. Section 3.1 will be the discussion of sapphire wafer fabrication with different approaches, and the comparison between them. Section 3.2 will give details design and procedure of sensor head fabrication. Evaluation and tests of the sensor heads will be illustrated in Section 3.3, with the comparison with theoretic analysis.

3.1 Fabrication of Sapphire Wafer

As we showed in Figure 2.4-2, the dimension of the desired wafer needs to fit in a $1mm$ diameter circle, and thickness would be as thin as possible to give higher fringe visibility. However, all the commercial available sapphire wafers are larger and thicker in both dimensions, the most close wafers from the market is about $75\mu m$ thickness, $1mm \times 1mm$ and $2mm \times 2mm$ square wafers[26]. In order to reduce both dimensions, it is necessary to polish and cut the wafers.

3.1.1 Wafer cutting

With currently available facilities, we have two methods to cut the sapphire wafers. One is through cutting by an ultrasonic cutter with titanium cutting tips; the other is dicing with a diamond linear saw, or diamond pen.

The mechanism of ultrasonic cutter, as shown in Figure 3.1-1, is by vibrating a circular cutting tip in a pool of diamond abrasive slurry. As the tool pushes down on the sapphire wafer, the vibration of the tool tip makes a cut through the wafer. Diamond slurry is applied in order to smooth the cutting process. During the cutting, we also used a syringe to press distilled water through the tool tip. The water flow can wash away the remaining dust from cutting, and also cool down the cutter and cutting area.

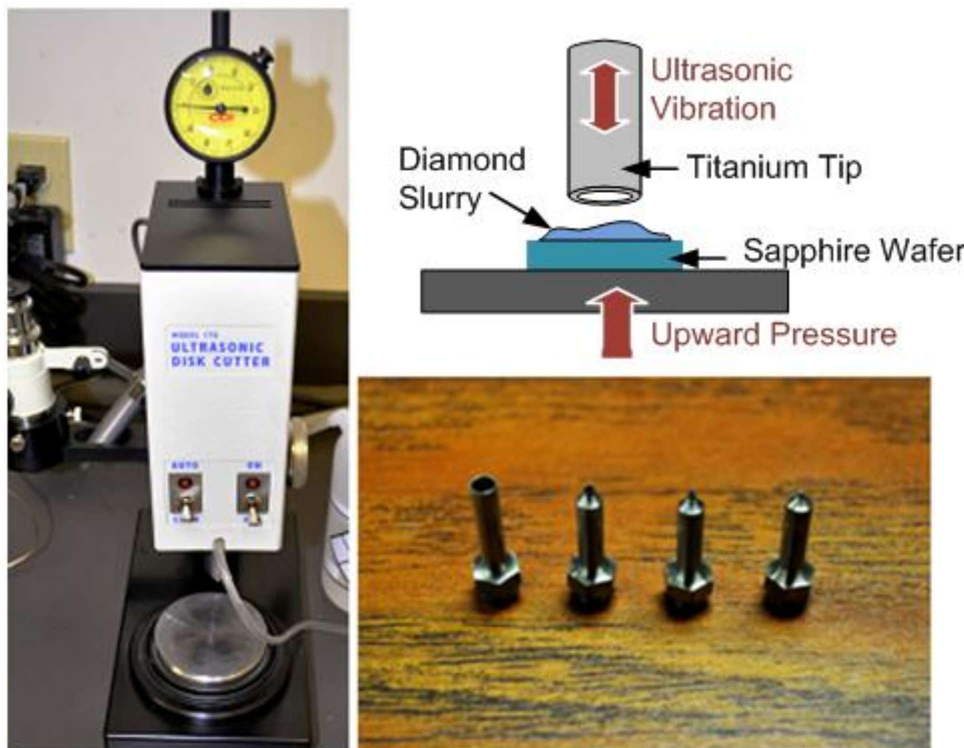

Figure 3.1-1 Ultrasonic Cutter

Left, ultrasonic cutting tool, upper right, conceptual diagram, lower right, titanium cutting tips

With cutting tips diameter ranging from $3mm$ down to $250\mu m$, we made a series of testing cuts on sapphire wafer of different thickness. The results are summarized in Table 3.1-1:

Table 3.1-1 Test results of ultrasonic cutter

Wafer Thickness	*Disc diameter*	*Result*	*Cutting speed*	*Tool wear rate*[1]	*Yield rate*	*Handling difficulty*
$300\mu m$	$3mm$	Success	7 min	8:1	99%	No difficulty
$300\mu m$	**$1mm$**	**Success**	**5 min**	**9:1**	**99%**	**No difficulty**
$300\mu m$	$500\mu m$	Stuck in the tip	3 min	10:1	90%	Little difficulty
$300\mu m$	$250\mu m$	Stuck in the tip	2.5 min	10:1	33%	Hard to retrieve from cutter
$75\mu m$	$1mm$	Cracked	N/A	N/A	≈ 0	Cracked during cutting
Notes:	1, the wear rate is defined as (thickness of wafer cut) : (length of tool lost)					

Although the cutter is designed to move in vertical direction only, horizontal vibration is inevitable. Such vibration would cause damage to the upper surface. Therefore, other techniques such as the bonding material, buffer layer as well as the handling during the cutting are used to improve the cutting procedure.

- Bonding material: Crystalbond 509 is used to bond the material onto the plate during cutting, which is proved to be stable and can be easily cleaned off with acetone. Merging the whole material into crystal bond will help to stabilize the cutter when it contacts the wafer surface, improve the upper surface quality, but also increase the cutting time, especially during cutting smaller wafers.

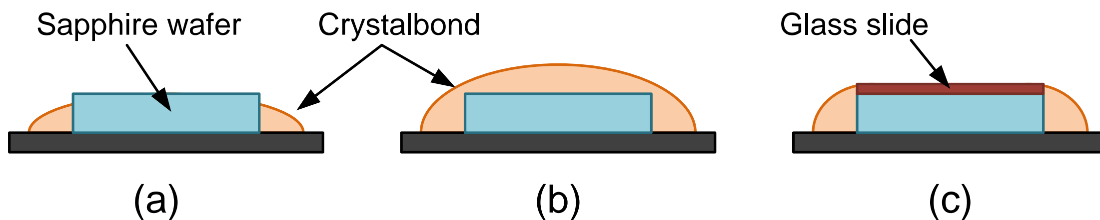

Figure 3.1-2 Methods to improve ultrasonic cutting
(a) weak bonding with wafer surface exposed, (b) strong bonding with wafer surface immersed, (c) surface protected by buffer layer ($160\mu m$ glass slide)

- Buffer layer: Theoretically adding a buffer layer on top of the material would help

improve the cutting quality of upper surface, since it can also help stabilize the cutting tip when it contacts the sapphire wafer surface. But our test showed very limited improvement and a large draw back at cutting speed (up to $\approx$40%)

Since the edge of sapphire wafer will not be used for sensing purpose, and considering the cutting speed and wearing rate, configuration (a) is chosen as the cutting solution for sapphire wafers over $300\mu m$. Figure 3.1-3 exhibits cut wafers of different size and Figure 3.1-4 shows $1mm$ sapphire disc under microscope.

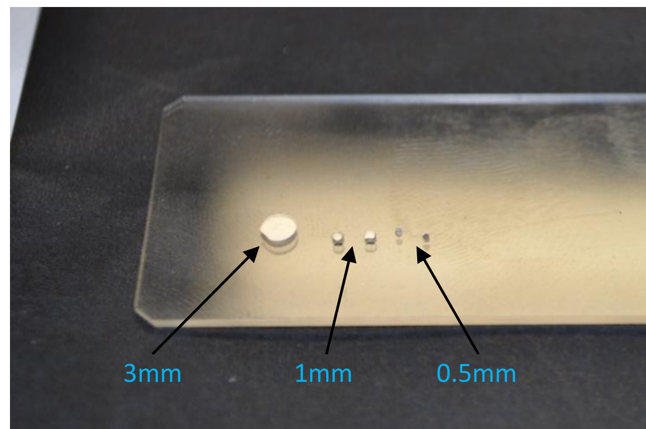

Figure 3.1-3 Sapphire wafers cut by ultrasonic cutter

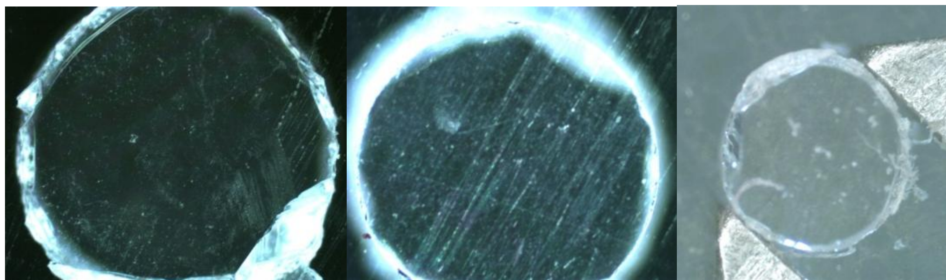

Figure 3.1-4 $1mm$ Sapphire disc under microscope
From left to right: Upper surface, bottom surface, measured by calipers

To summarize the cutting method with ultrasonic cutter, it is able to manufacture circular sapphire discs with rough edges. However the thickness of cut wafer is limited to thick wafers ($> 200\mu m$), thin wafers under $100\mu m$ can hardly survive the cutting procedure. Further polishing is needed if we follow this method.

The dicing method requires different tools for different wafer thickness. For sapphire wafer over $300\mu m$ a diamond-based linear dicing saw is required. And the dicing process is more complicated, it is carried out by professionals of material science. However, for thinner sapphire wafers below $100\mu m$, it is able to dice the wafer with diamond pen. But for both approaches, the diced wafer would be rectangular or square shaped, rather than the ideal circular case.

The dimension of the diced wafer needs to be able to fit the sensor head design, which contains an inner and an outer tube (Figure 2.4-2). The inner tube we used for the project has a diameter of $\approx 1.2mm$, it has four holes to hold the sapphire fiber, Left figure of 3.1-5 shows the hole distribution in the tube.

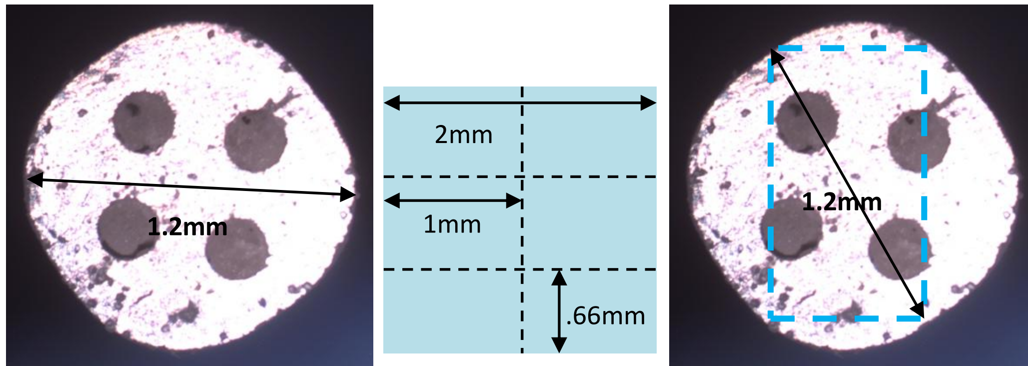

Figure 3.1-5 Dicing Wafer to Fit in the Inner Tubes

left, inner tube dimension; middle, wafer dicing dimension; right, put wafer onto the tube

In order to fit in the $1.2mm$ diameter circle, and cover at least one hole of the tube. We started with the $2mm \times 2mm$ square wafer, and intend to dice it into six pieces of $1mm \times 0.66mm$ rectangular wafers, as shown in the middle figure of 3.1-5, the diagonal of each piece is about $1.2mm$. After putting the wafer onto the inner tube, we expect a scheme like the right figure of 3.1-5.

During the dicing procedure, we first prepared a paper with grids with exact size of $1mm \times 0.66mm$ rectangular (Figure3.1-6), taped firmly on a table. Then we place the wafer on the paper, adjust the position to fitting the grids, use one piece of metal to press the wafer down, preventing it from any movement, the side of the metal piece is aligned with the cutting line. After all the alignment, we use a diamond pen to slice

gently along the edge of the metal piece, with small amount of pressure force. After several times of slice, the wafer would be cut. In order to finely control the dicing procedure, all these steps need to be carried out under microscope, as shown in Figure 3.1-6.

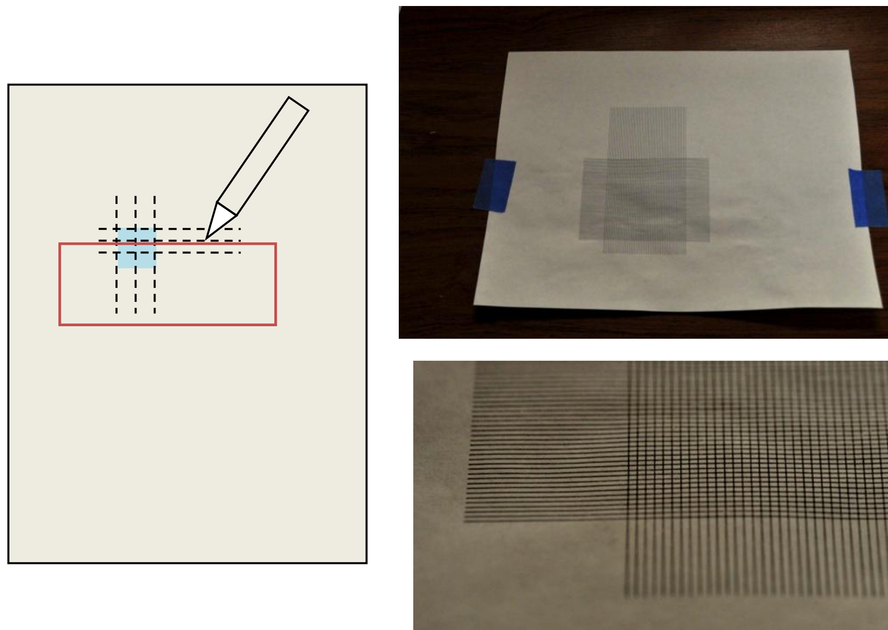

Figure 3.1-6 Wafer Dicing Process

Left, a conceptual illustration of dicing process, upper right, the paper used with grids on, bottom right enlarged grids

To summarize the dicing method, thick wafer dicing is complicated and costly, and the diced wafers still need to be polished. But for thinner sapphire wafer below $100\mu m$, the dicing procedure can be easily achieved within the laboratory. Although the diced sapphires are not ideal circular shape, they are still able to cover the holes on inner tube, which is sufficient for sensing purpose.

3.1.2 Wafer Polishing

The polishing method we use for thinning the wafers is mechanical polish. The wafer is attached to a flat platen within a grinder with crystal bond, then slowly grinded on a polish machine with diamond powder coated polishing paper (Figure 3.1-7).

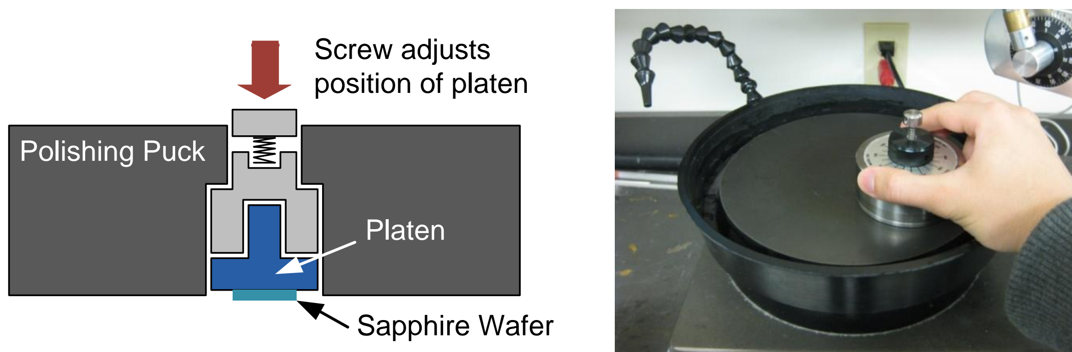

Figure 3.1-7 Wafer Polishing
Left, conceptual diagram of grinder with wafer bonded, right, grinding on a polish machine

As we discussed in Chapter 2, the thickness of wafer largely determines the fringe visibility. In addition to that, the fringe visibility of sapphire based wafer is very sensitive to the wedge angle and parallelism. Figure 3.1-8 is the experimental data of the wafer quality. Although the experimental data does not totally agree with Figure 2.3-6 due to the different FP cavity and interrogating fiber type, they follow the same trend that thinner wafer gives better fringe visibility result.

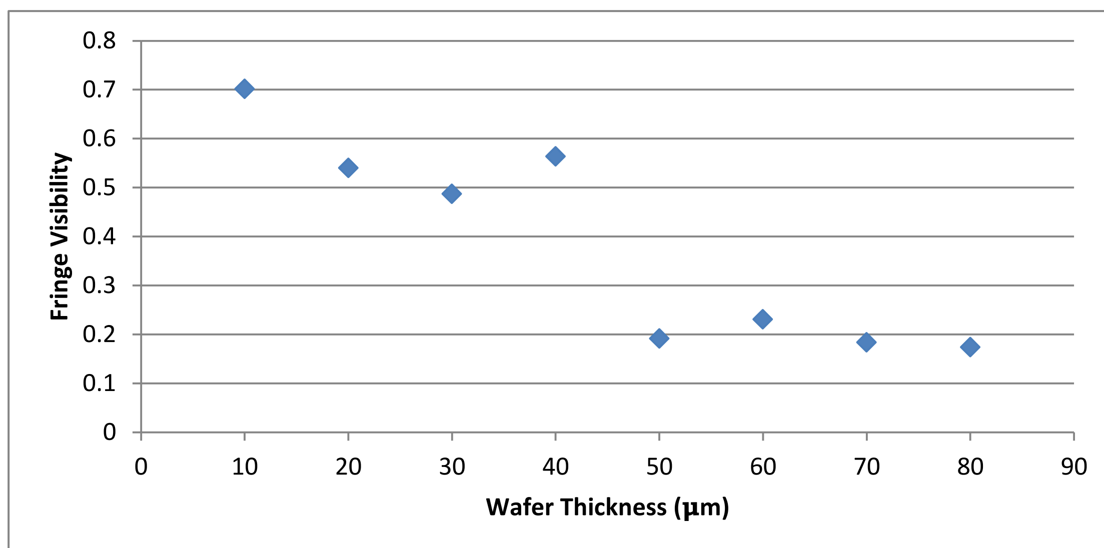

Figure 3.1-8 Experimental Result of Sapphire Wafer Polishing[27]
Based on MMF with core diameter $100\mu m$, FP cavity: sapphire wafer ($n \approx 1.7$)

3.1.3 Finalization of Wafer Fabrication

Combine all the wafer cutting and polishing techniques with the sapphire wafers types in stock, the advantages and disadvantages are listed in Table 3.1-2.

Table 3.1-2 Comparison of Sapphire Wafer Fabrication Procedure

Wafer Type	Thick ($> 300\mu m$)	Thin($< 100\mu m$)
Ultrasonic cutting	Achievable: Yes Advantage: Circular, dimension match	Achievable: No
Dicing	Achievable: Yes Disadvantage: Costly procedure Rectangular, dimension mismatch	Achievable: Yes Disadvantage: Rectangular, dimension mismatch
Polishing	Achievable: Yes Disadvantage: Low fringe visibility Time consuming procedure	Achievable: Yes Advantage: High fringe visibility Disadvantage: Irregular shaped wafers

From Table 3.1-2, we finalized our sapphire wafer fabrication approach. Starting with $2mm \times 2mm$ sapphire wafer of $75\mu m$ thickness, we first polish the wafer down to around $30\mu m$. Since some of the wafers may be cracked into irregular shapes, we just need to dice the pieces sufficiently fit onto the inner tubes, and discard the pieces too small to cover one hole on inner tube. Figure 3.1-9 demonstrates some of the sapphire wafers fabricated in this routine.

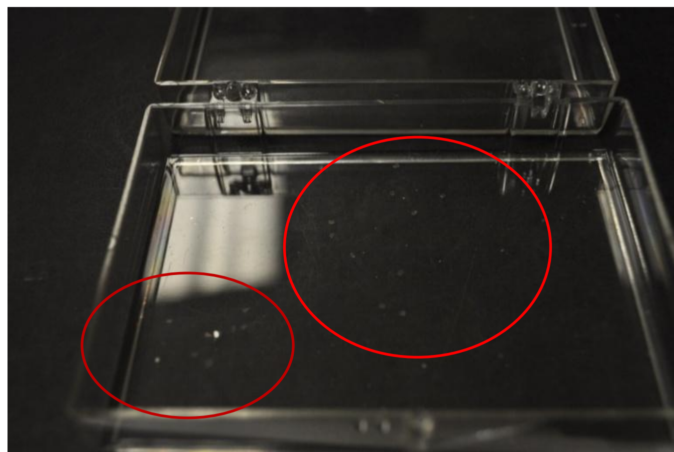

Figure 3.1-9 Sapphire Wafers Fabricated

3.2 Sensor Head Assembly

The assembly of the sensor head is the procedure to stabilize the sensing components, i.e. the sapphire wafer, and to guarantee a steady connection between the wafer and the inserted fiber later on. Our sensor head design, as shown previously in Chapter 2, involving two kinds of alumina tubes, will permanently attach the sapphire wafer onto one end of the inner tube, then inserted into the outer tube. For sealing the outer tube, we have several approaches,

- First approach is to insert the inner tube (with sapphire wafer on it) into the outer tube first, and then use CO_2 laser to seal the end of outer tube.
- Second approach is to seal the outer tube first, with either CO_2 laser or Oxy-acetylene torch, then insert the inner tube with sapphire wafer into the outer tube.
- Third approach is similar to the first one, except we do not seal the outer tube. Instead, alumina adhesive is applied to fill the remaining space.

All the three approaches have been experimented, and they could achieve similar fringe visibility with accurate and careful handling. Additionally, different wafers are used which would result fringe visibility difference. So the final sensor heads we used in our sensor links are selected by comparing their fringe visibilities.

3.2.1 Wafer Attachment

Regarding which approach to assemble the sensor, it is a crucial step to attach the wafer onto the inner tube, with at least one hole fully covered. Figure 3.2-1 shows the setup used to finely adjust the wafer and applying glue for the attachment. The inner tube is placed into a hole on the metal base with narrow tolerance, in order to keep the tube firm and straight. The needle which is connected with a translation stage can be accurately adjusted in three dimensions is used to modify the wafer position on the tube and also to apply pin-down force to press the wafer stable when applying glue. Microscope is also needed to monitor the whole assembly process.

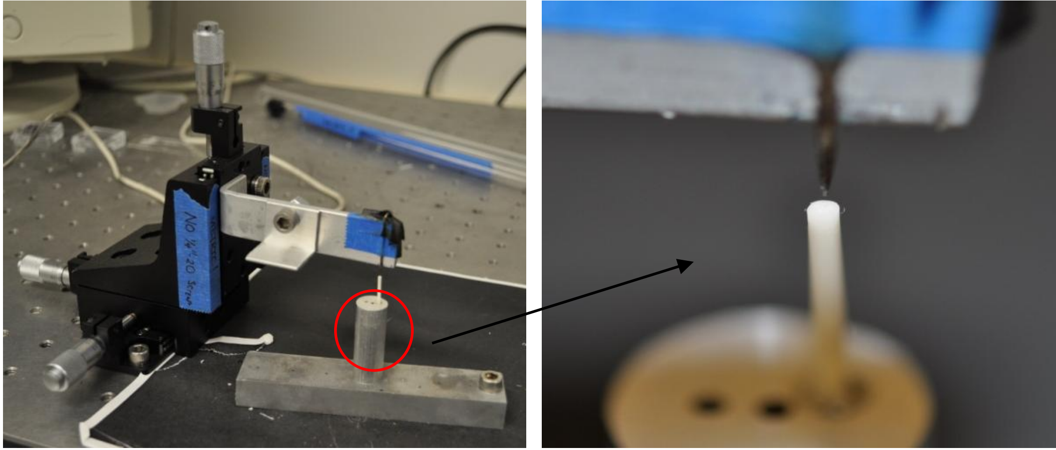

Figure 3.2-1 Sensor Assembly Setup

Ideally, all the adhesives we used to glue the sapphire wafer onto the tube and other attachment during sensor head manufacture would be alumina adhesive, in order to maintain the consistency of material. However, since the alumina adhesive usually comes along with water solution, direct applying adhesive to the wafer and tube joint may risk the sensing components. Due to the capillary action, the solution will go beneath the wafer into the holes, which may block the hole or stain the sapphire wafer surface after the adhesive is cured. Therefore, before the alumina adhesive, we would apply glue on the sides of the wafer, to prevent adhesive solution from sinking into the holes later on. The glue needs to have less fluidity at room temperature, and needs to be burned out at high temperature. Sol-gel and phenyl salicylate (epoxy) is used for this purpose.

Starting with a polished inner tube, placed in the hole of metal base as shown in Figure 3.2-1, we then adjust the microscope to focus on the top surface of inner tube. Next step is to use the vacuum tweezers to pick up a dice sapphire wafer, and lay it onto the tube. Adjust the needle horizontally to precisely control the position of the sapphire wafer, and then pin down the needle vertically to stabilize the wafer. Once the wafer is pressed on the tube firmly, we use a short piece of optical fiber to apply Sol-gel along the side of the wafer. We need to minimize the amount of Sol-gel used to limit the capillary action because direct contact between Sol-gel and the sensing surfaces will degrade the fringe visibility. Then we use a heat gun for fast curing of Sol-gel, once the Sol-gel becomes mostly solid, the pin-down is released, and the

inner tube is placed in a furnace for regular Sol-gel curing procedure, as shown in Table 3.2-1.

Table 3.2-1 Adhesive Curing Procedures

Adhesive Type	Sol-gel	Alumina Adhesive (Resbond 903 HP)
Start at	100℃	Room temperature
Ramping	To 250℃, with $3℃/min$	To 120℃
Dwelling	30 min	2 hours
Ramping	To 600℃, with $3℃/min$	To 371℃ (700°F)
Dwelling	30 min	4 hours
	Turn off	Turn off

3.2.2 Laser Sealing Technique

Laser sealing of the outer tube provides extra protection to the sapphire wafer, and thermal fusion conjunctions are more endurable than sticking together by adhesives. However, the CO_2 laser we possess is not powerful enough to melt the outer tube end, alumina balls and circular alumina layers are used as a cap on the outer tube. By thermally fusing the junction between the cap and the tube edge, the outer tube can be sealed firmly.

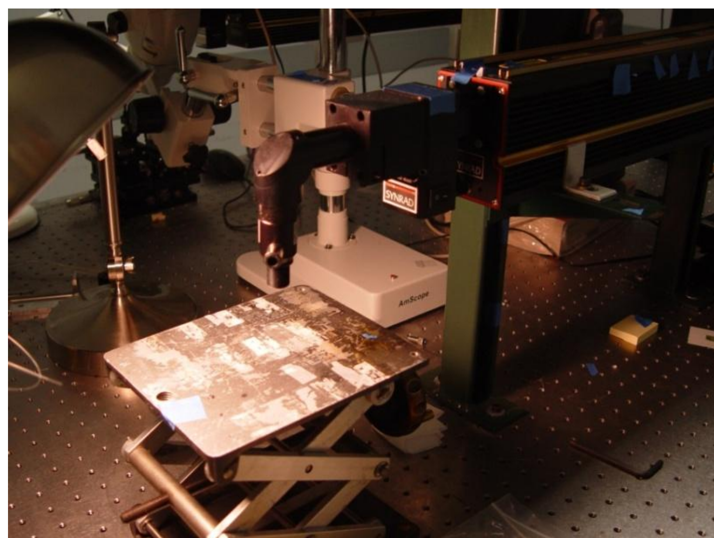

Figure 3.2-2 Laser Sealing Setup

The setup for the sealing procedure is shown in Figure 3.2-2. The CO_2 laser is focused by a cylindrical lens with $5cm$ focal length. The translation stage is adjustable vertically to match the focus point of laser onto the outer tube. The tube is placed on an adiabatic stand to prevent too much loss of thermal energy into the stand. The operation of CO_2 laser is precisely controlled by a computer through serial port, a microscope can also be used to monitoring the sealing procedure in real-time.

As for the fabrication of cap material, the circular alumina layers are cut out from large alumina pieces ($400\mu m$ thickness), with the ultrasonic cutter, due to the size mismatch (the cut disc is $1mm$ in diameter, while the hole of outer tube is $\approx 1.2mm$), more than one alumina layers are used. The alumina ball is made by melting alumina powder with CO_2 laser, with the similar setup in Figure 3.2-2. Experimentally we found direct focusing laser on to a pile of alumina powder will melt the powder and form an alumina ball due to the surface tension. The ball size is determined by the power of laser, slightly affected by the duration of exposing to laser. With CO_2 laser of $8\sim9W$, exposing for 10 second, the alumina powder could form a ball slightly bigger than the hole, which serves nicely as a cap.

After the cap mounted onto the tube, higher power and longer duration of CO_2 laser is used (for alumina ball, laser power is 25W and $30\sim60sec$ exposing time; for alumina layers, laser power is 25W and $10\sim20sec$ exposing time). The sealing result is shown in Figure 3.2-3.

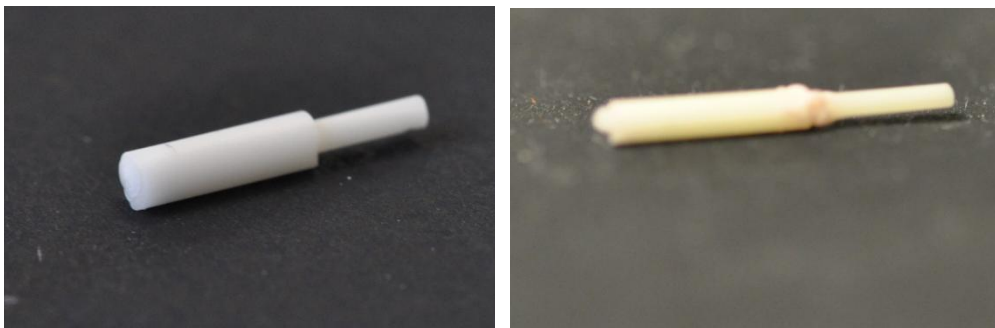

Figure 3.2-3 Sealed Sensor Heads

Left: sealed with alumina layers, right: sealed with alumina ball

3.2.3 Final Assembly and Loss Analysis

Alumina adhesive is used when inserting the inner tube (with sapphire wafer attached) into the outer tube, and additional alumina layer ($\approx 400\mu m$) is used to serve as a buffer layer between the sapphire wafer and outer tube end. The purpose of the buffer layer is to stabilize the sapphire wafer position even if the Sol-gel/ phenyl salicylate is totally burned out, and also to protect the thermal power from directly hitting the wafer during the laser sealing and later in the sensing environment. Applying the alumina adhesive could be either before or after the sealing procedure, depending on which approach is followed, and the curing process is necessary right after applying alumina adhesive. The Curing procedure is listed in Table 3.2-1 above.

The loss of fringe visibility during the sensor head assembly may appear in each step:

- Due to the capillary action, small amount of sol-gel could sink into the holes or stain the back side of the sapphire wafer, degrading the fringe visibility. Loss during applying sol-gel largely depends on the handling.
- Loss during applying alumina adhesive is very small and could be neglected.
- Loss during laser sealing are introduced when the outer tube is sealed with the inner tube and wafer already inserted. It is most likely due to the local thermal heating that causes the displacement even distortion of the sapphire wafer. Using multiple or thicker buffer layer could reduce the loss of this kind.

All three of the approaches have some combination of the losses:

Table 3.2-2 Loss Analysis of Sensor head Assembly

	1st Approach	2nd Approach[1]	3rd Approach[2]
Wafer attachment	phenyl salicylate	Sol-gel	Sol-gel
Loss	Non-detectable	1~3dB	1~3dB
2nd Step	Insert outer tube Alumina adhesive	Seal outer tube	Insert outer tube Alumina adhesive
Loss	<3dB	0	<1dB
3rd Step	Laser sealing the outer tube	Insert outer tube Alumina adhesive	N/A

Loss	1~3dB	<1dB	0
Total Loss	2~6dB	2~4dB	1~4dB
Notice	1, the concern about 2nd approach is mainly at step 3, where the insertion may remain some air trap between outer tube and sapphire, which may give space for wafer to move especially when Sol-gel is burned out at high temperature. 2, potential problems of the 3rd approach: • The space left when phenyl salicylate is burned out, since it is organic with only carbon, hydrogen and oxygen, which would leave gases only. • Without sealed outer tube, the sensor could be more vulnerable in the sensing environment		

3.3 Sensor Head Evaluation

An interrogation system is used to evaluate the sapphire wafer and fabricated sensor heads (Figure 3.3-1). The system is similar to the conceptual diagram shown in Figure 2.5-1.

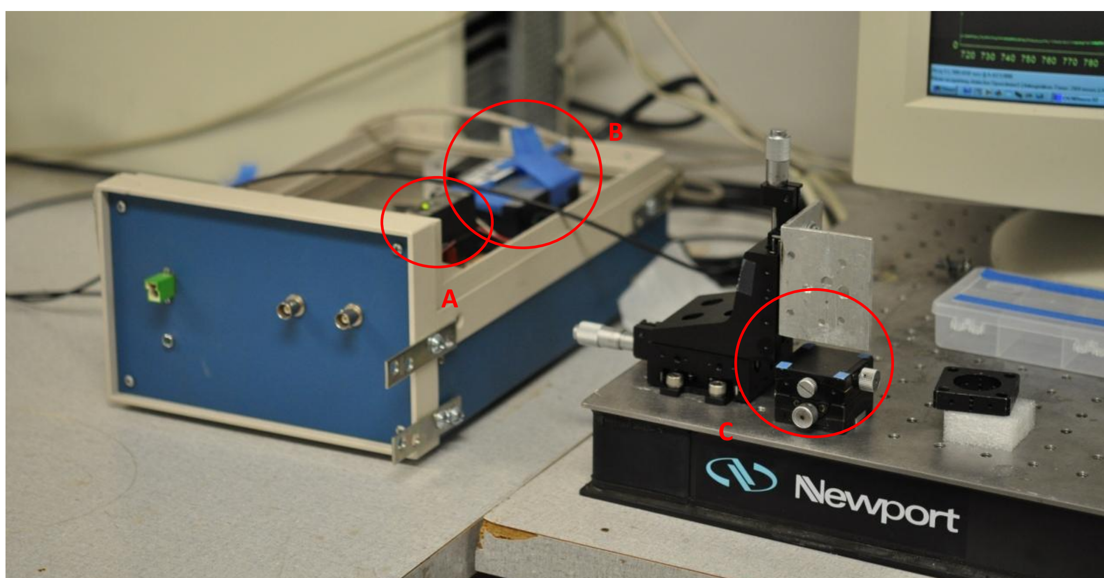

Figure 3.3-1 Sensor Head Interrogation system

A, the laser diode; B, the OcceanOptics spectrometer; C, the translation stage for finely tuning the interrogating fiber towards sapphire wafer

For the interrogation of sapphire wafers, a multimode silica fiber is bonded vertically onto the aluminum platen connected with the translation stage. With the help of a microscope, we can interrogate multiple points on a single wafer by adjusting the fiber position. Silica fiber is used here instead of sapphire fiber because sapphire fiber is extremely fragile and easy to break. The handling especially the bonding process could largely risk the fiber.

Sensor head interrogation does not require the translation stage. Instead, the sensing sapphire fiber is directly inserted into the sensor head. Spectrum of sensor heads after each step is taken for fringe visibility calculation, which contributes to the result in Table 3.2-2.

The sensor heads selected for a sensor link used 1st and 3rd approach, their final fringe visibility of the sensor heads after $1200℃$ annealing is 0.2 and 0.18. Table 3.2-3 records the fringe visibility degradation of these two sensor heads. The annealing process intends to release the thermal strength within all the adhesive attachment, also burned out some of the Sol-gel material, which is one cause of slight increase in fringe visibility.

Table 3.3-1 Fringe Visibility during Sensor Head Fabrication[1]

Approach	Start FV	Wafer Attachment		2nd Step		3rd Step		Annealed
1st	0.57	phenyl salicylate	N/A	Alumina adhesive	0.197	Laser Sealing	0.163	0.234
3rd	≈ 0.4	Sol-gel	0.20	Alumina adhesive	0.177	N/A	0.177	0.18
Note	The fringe visibility of starting wafers was measured using silica MMF, for the reason explained previously. Rest of the fringe visibility measurements were taken with a piece of $50cm$ sapphire fiber, which is about the length of sapphire fiber in the final sensor link.							

Chapter 4.

Sensor Link Assembly and Signal Processing

The fiber chain connection between the sensor head and the interrogation system is referred as sensor link, whose function is guiding light to and from the FP cavity. Due to the harsh sensing environment we discussed in Chapter 2, at least part of the sensor link would be surrounded with high temperature. Sapphire fibers are able to resolve the difficulty with high temperature capability, but also raise some new challenges for interrogation.

In this chapter, we will analyze the loss of sapphire fiber experimentally in Section 4.1, in order to determine the sapphire fiber length used in the sensor link. Section 4.2 will discuss the angle polishing and splicing method for silica-to-sapphire fiber connection, which is proven to reduce the reflection at splicing point and therefore preserve the fringe visibility. And then, the procedure of sensor link assembly will be explained in Section 4.3. Section 4.4 will explain the signal processing method to calibrate the sensor.

4.1 Experimental Measurement of Loss in Sapphire Fiber

Due to the highly multimoded nature, and without cladding, sapphire fiber usually has higher loss than normal multimode silica fiber. The loss of sapphire fibers differs from the fiber diameter and growing technique. However, the loss data provided by the manufacturer of the sapphire fiber could not match the loss that we have observed in experimental analysis of reflection at a silica-to-sapphire splicing point (see next section). We decided to measure the loss of sapphire fiber through a relatively simple

experiment.

The experiment setup is shown in Figure 4.1-1, where R_1 is the reflection coefficient at the splicing point, R_2 is the reflection coefficient at the interface between sapphire fiber and index matching liquid.

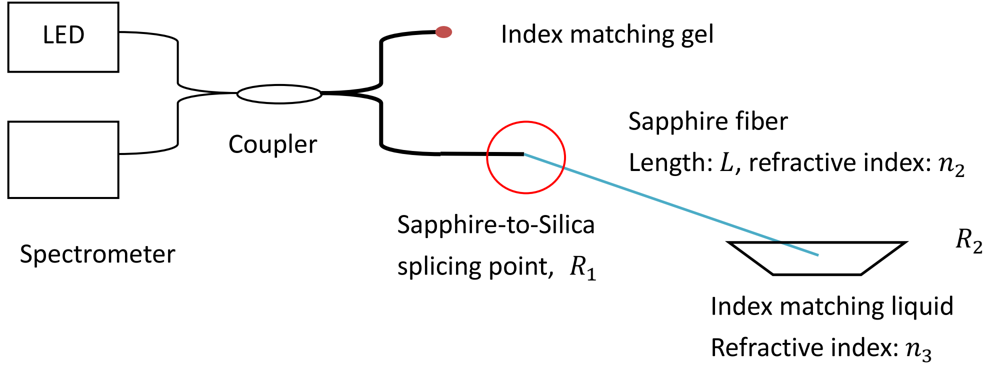

Figure 4.1-1 Experiment Setup for Loss Measurement in Sapphire Fiber

Assuming the light intensity from LED is I_0 and the coupler used in the system is a 3dB coupler, then the light collected at the spectrometer I_{TOT} can be described by Equation 4-1.

$$I_{TOT} = \frac{1}{4}(I_0 R_1 + I_0 T_1^2 R_2 A) \tag{4-1}$$

Here T_1 is the transmitted light from silica fiber into sapphire fiber, and A is the loss in sapphire fiber. Assuming the loss is consistent for given length of sapphire fiber, we have $A = e^{-2\alpha L}$, where α is a constant. In Equation 4-1, R_2 can be defined by Fresnel equation, $R_2 = \left(\frac{n_2 - n_3}{n_2 + n_3}\right)^2$, I_0 and R_1 are unknown. Fiber length L and refraction coefficient of the index matching liquid n_3 is adjustable to generate equations. We have three unknowns in the equation, and need at least three different combination of L and n_3 to calculate the value of α.

$$\begin{cases} \beta_1 = \dfrac{I_{TOT}^{(1)}(n_3)}{I_{TOT}^{(2)}(n_3)} = \dfrac{R_1 + I_0 T_1^2 R_2(n_3) e^{-2\alpha L_1}}{R_1' + I_0 {T_1'}^2 R_2(n_3) e^{-2\alpha L_2}} \\ \beta_2 = \dfrac{I_{TOT}^{(1)}(n'_3)}{I_{TOT}^{(2)}(n'_3)} = \dfrac{R_1 + I_0 T_1^2 R_2(n'_3) e^{-2\alpha L_1}}{R_1' + I_0 {T_1'}^2 R_2(n'_3) e^{-2\alpha L_2}} \end{cases} \tag{4-2}$$

Typical spectrum from this setup is shown in Figure 4.1-2. The ratio β value can be calculated by picking the intensity data on same wavelength. Here we picked $850nm$ which is around the peak value of light intensity.

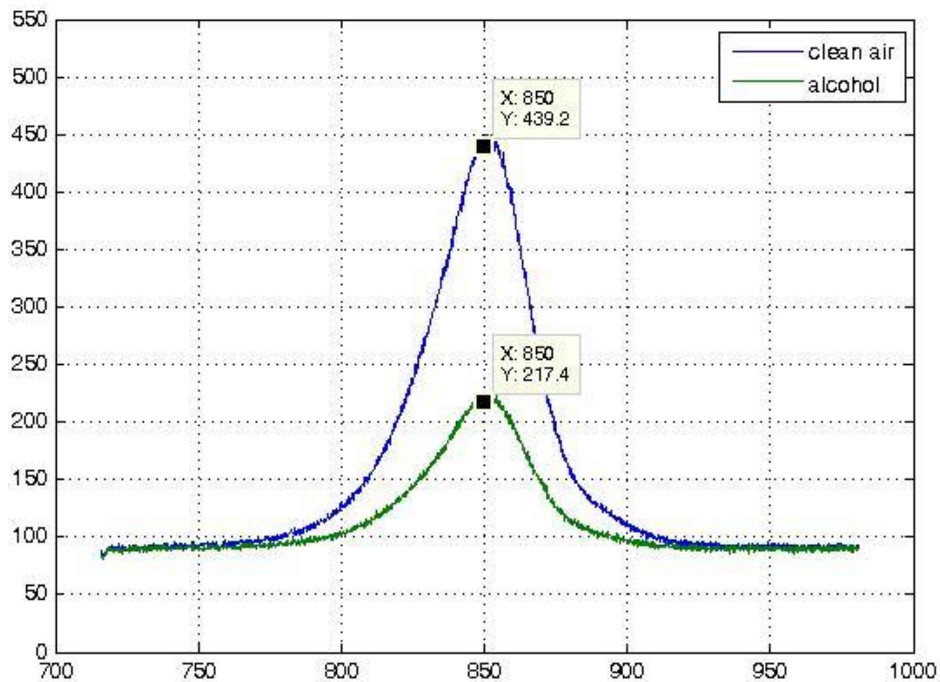

Figure 4.1-2 Spectrum Data for Loss Measurement

While solving Equation 4-2, two assumptions are made:

- $R_1 = R_1'$ and $T_1 = T_1'$, which means the reflection at splicing point is the same for different lengths of sapphire fibers. This assumption may not be valid when different sapphire-to-silica splicing is used.
- $T_1 = 1 - R_1$, which indicates at the splicing point, the light is either reflected by the sapphire fiber end or transmitted into the sapphire fiber. This assumption neglects the loss at the splicing point.

The numerical solution for Equation 4-2 gave the value of α from 0.0041 to 0.016, with variance over 0.005. Such inaccuracy mostly came from the assumptions we made, especially the second assumption. As we mentioned in Chapter 2, the splicing point usually involves certain loss from the mode mismatching and light leaking, which should not be neglected. Therefore, T_1 is an additional unknown and more equations are needed. However, numerically solving for more unknowns is time consuming and also brings in more uncertainty. Therefore a different approach of curve fitting is used.

Recall Equation 4-1, including all the unknowns we can simplify it into a normalized

form,

$$I_{normal} = a + c \times e^{-2b \times L} \tag{4-3}$$

where a, b and c are all unknowns and the sapphire fiber length L is a variable. The curve fitting is based on the assumption that all the unknowns remain constant during variable changes. This assumption can be easily satisfied if we never break the splicing point when shortening the sapphire fiber, and polishing the fiber end each time after shortening. The curve fitting result is shown in Figure 4.1-3. We used different index matching liquids (clean air and alcohol) to generate two curves for fitting, and their results agree with each other. The fitting result is 0.304dB loss per centimeter.

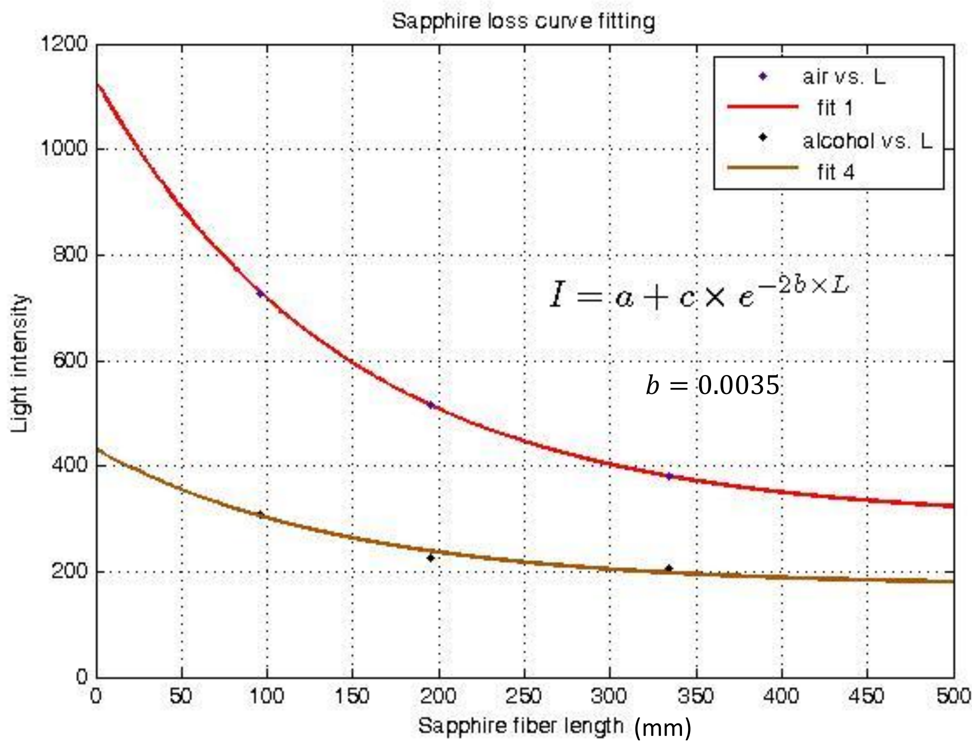

Figure 4.1-3 Curve Fitting Method for Loss Measurement

4.2 Silica-to-Sapphire Fiber Splicing

As previously discussed in Chapter 2, the silica-to sapphire splicing is different with normal silica-to-silica fiber splice. Instead of melting two fiber ends and pushing them

to joint together, we melt only the core of the multimode silica fiber and insert the sapphire fiber into it. Core-doped multimode fiber is selected for this splicing since doped core has lower softening temperature than the cladding. Splicing conditions are carefully controlled so that the cladding remains solid and function as a tube while the core is softened and the sapphire fiber can be inserted in. Different splicing conditions are tested and the finalized parameters are listed in Table 4.2-1

Table 4.2-1 Splicing Parameters for Silica-to-Sapphire Splicing (Sumitomo Type36)

ARC Duration	0.3 sec
Prefusion	0.1 sec
ARC Gap	0 μm
Overlap	0 μm
Power	1 step

Due to the low power and the short arc duration used, repeating arc is needed to make sapphire fiber fully embedded into silica fiber. Figure 4.2-1 shows a typical silica-to-sapphire fiber splicing.

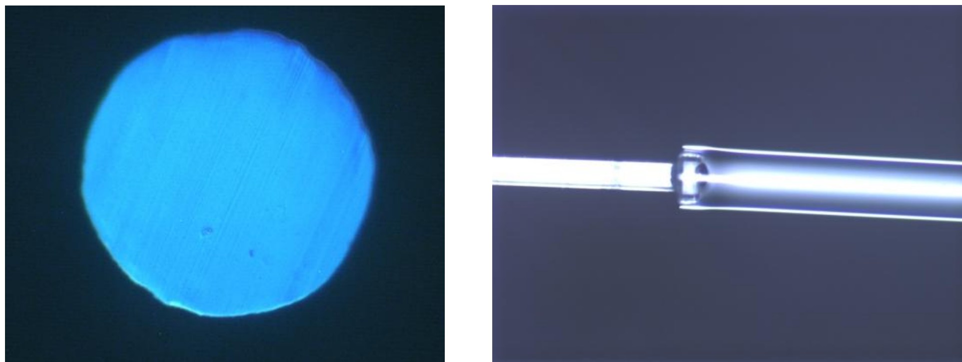

Figure 4.2-1 Silica-to-Sapphire Splicing
left: polished sapphire fiber, right: spliced fiber under microscope

However, such splicing could cause huge loss in light intensity and degradation to fringe visibility, mainly for the following reasons:

- Mode mismatching

Although we use multimode fiber (MMF) to splice with sapphire fiber, there would still be mode mismatching between them, due to the highly multimoded nature of sapphire fiber, and the difference in numerical aperture (NA). Such mismatch would cause loss at the splice point.

- Light leaking from silica fiber

Due to the difference in diameters of the core of silica fiber and sapphire fiber, leakage would happen to the light coming from the silica side. Such leakage would further decrease the light intensity that goes into the sapphire fiber.

- Reflection at sapphire fiber

Since the sapphire fiber is not melted or deformed during the splicing procedure, the reflection at the silica-to-sapphire interface is inevitable. The reflection not only diminishes the interference signal from sapphire fiber and sensor head, it also raises the background of the spectrum, which will further compromise the quality of interference pattern.

- Air gap

As shown in the right figure of 4.2-1, beyond the head of sapphire fiber inserted into silica fiber, a bubble shape of gap is formed. Such air gap could cause large reflection at the splicing point, even greater than the reflection from sapphire fiber end. The air gap usually forms because of defect on surfaces of the two fiber end. Either poorly polished sapphire fiber or unsuccessful silica fiber cleaving could lead to such an air gap.

Base on the potential causes of loss and fringe degradation at the splicing point, a new idea is proposed to partially solve the problem. Like a standard angle-polished connector (APC) for single-mode fiber, it is thought that introducing an angle to the end of sapphire fiber could cause some of the reflected signal to couple into leaky modes, thereby attenuating the reflection before it reaches the spectrometer. However, due to the large acceptance angle of multimode fiber, big polishing angle may be necessary.

Additionally, the angled sapphire fiber end could present a better configuration for insertion into the softened silica fiber core. Just like a knife edge, the angled sapphire

fiber could penetrate more deeply and easily into the core of silica fiber. Such configuration could also help to reduce the chance of appearance of the air gap (Figure 4.2-2) and therefore produce a higher quality splice.

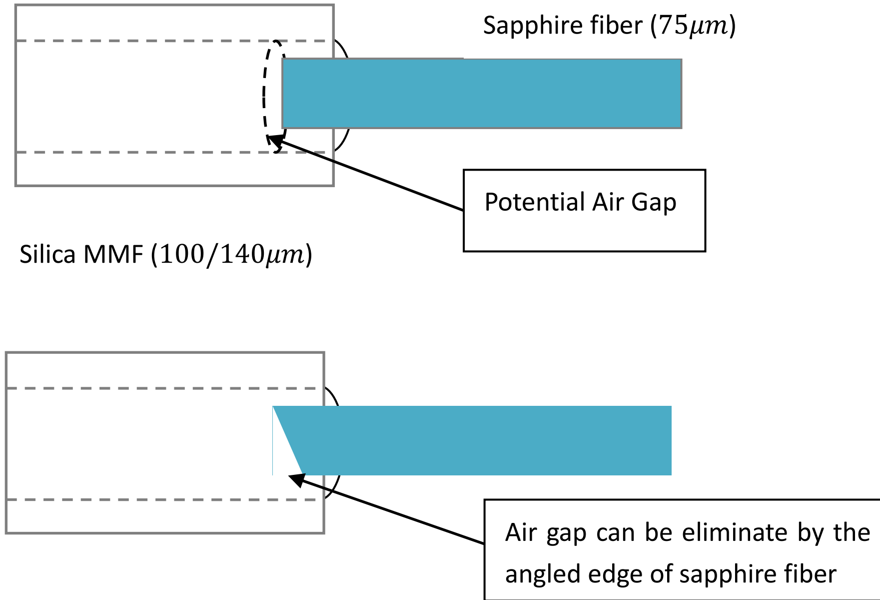

Figure 4.2-2 Comparison between Normal Splice with Angled Splice

Different polishing angles are tested and the setup shown in Figure 4.1-1 was used to quantitatively analyze the reflection at splicing point. Adopt from Equation 4-1: $\mathrm{I} = \frac{1}{4}(I_0 R_1 + I_0 \mathrm{T}_1^2 R_2 A)$, where I_0, R_1 is unknown and $R_2 = \left(\frac{n_2 - n_3}{n_2 + n_3}\right)^2$. For two different index matching liquids, we have different R_2, namely R_2 and R_2'. Then I_0 can be cancelled out by combining two equations together:

$$\frac{I_1}{I_2} = \frac{AR_2(1-R_1)^2 + R_1}{AR_2'(1-R_1)^2 + R_1} \quad (4\text{-}4)$$

After rearranging the above equations, we have:

$$R_1^2 + (C-2)R_1 + 1 = 0 \quad (4\text{-}5)$$

where $C = \frac{I_1 - I_2}{A(I_1 R_2' - I_2 R_2)}$ can be calculated from experimental data.

Figure 4.2-3 shows the combined spectrum results of reflection with 10° angle splicing, where different colored curve represent different index matching liquid (the refraction index is listed in the brackets). Several combination of data sets are used to

calculate an average value for R_1, as shown in Figure 4.2-4. 10° and 15° degree splicing showed significant improvement by reducing the reflection at the splicing point to ≈ 0.01.

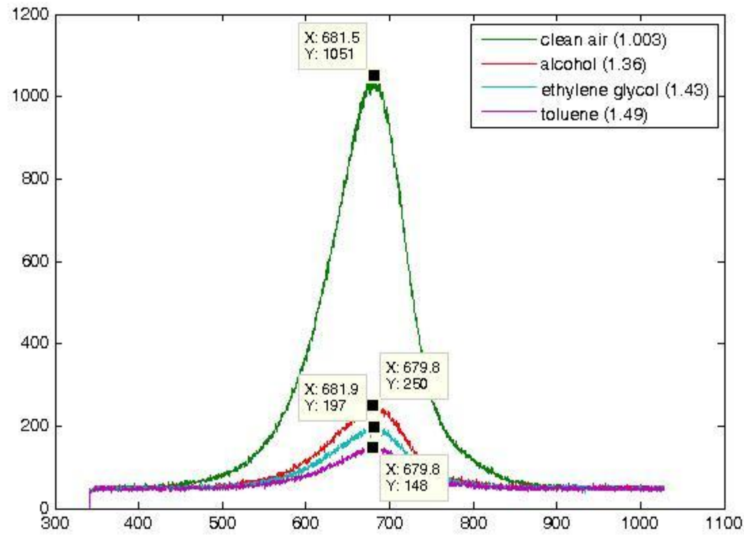

Figure 4.2-3 Reflection Spectrum with 10° Angled Splicing

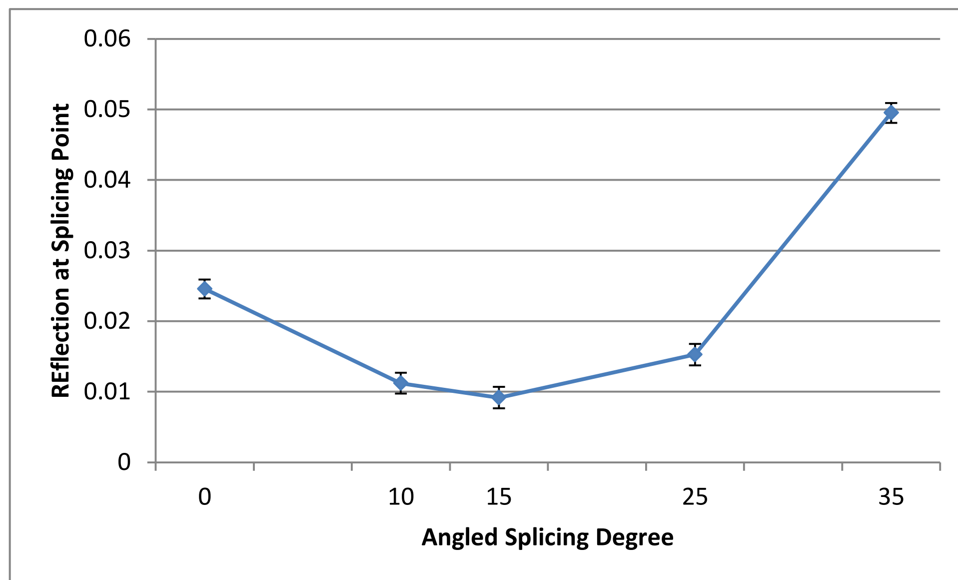

Figure 4.2-4 Reflection versus Angled Splicing Result

Among all the causes of loss at the splicing point, the reflection determines the quality of the splice and mostly affects the fringe visibility. Simulation has been done based on the configuration of Figure 4.2-5.

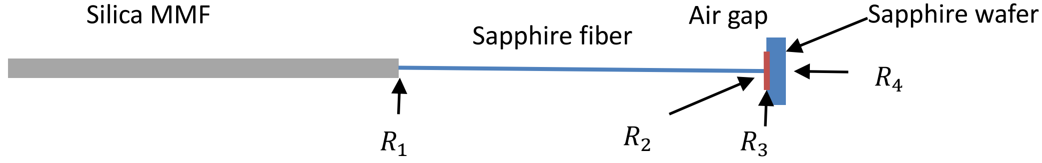

Figure 4.2-5 Configuration of Simulation for Fringe Visibility versus Reflection

Here R_1 through R_4 correspond to the reflection coefficients between: MMF and sapphire fiber, sapphire fiber and the air gap, air gap and the sensing wafer, and the end of the wafer with air. It should be noted that the air gap included here is for better approximation of experiment, since in reality air should always exists between the sapphire fiber end and the wafer, it brings in more reflections for consideration. Assuming the incident light into the MMF is I_0, the reflected light of each interface can be expressed as:

- Splicing point: $I_0 R_1$
- Sapphire fiber to air gap: $I_0 T_1^2 R_2 A$
- Air gap to sapphire wafer: $I_0 T_1^2 T_2^2 R_2 A$
- Wafer end: $I_0 T_1^2 T_2^4 R_2 A$

Noticing here we have $R_2 = R_3 = R_4 = \left(\frac{n_{sapphire} - n_{air}}{n_{sapphire} + n_{air}}\right)^2$ since they are all reflection between air and sapphire, and A is the loss in sapphire fiber. The total reflected light is the sum of all the four reflections, and reflections at R_3 and R_4 will form the F-P interferometer. Fringe visibility can be calculated by Equation 2-8: $FV = \frac{I_{max} - I_{min}}{I_{max} + I_{min}}$, where the maximum and minimum comes from the superposition of $I_0 T_1^2 T_2^2 R_2 A$ and $I_0 T_1^2 T_2^4 R_2 A$. Therefore we have:

$$\begin{cases} I_{max} = I_0 R_1 + A I_0 T_1^2 R_2 + A\left(\sqrt{I_0 T_1^2 T_2^2 R_2} + \sqrt{I_0 T_1^2 T_2^4 R_2}\right)^2 \\ I_{min} = I_0 R_1 + A I_0 T_1^2 R_2 + A\left(\sqrt{I_0 T_1^2 T_2^2 R_2} - \sqrt{I_0 T_1^2 T_2^4 R_2}\right)^2 \end{cases} \quad (4\text{-}6)$$

With the loss of sapphire fiber we get from Section 4.1, we can plot the relationship between R_1 and fringe visibility (Figure 4.2-6). It is clearly shown in the figure that especially for longer fiber, reduction of reflection at splicing point could largely

preserve the fringe visibility of sensing wafer.

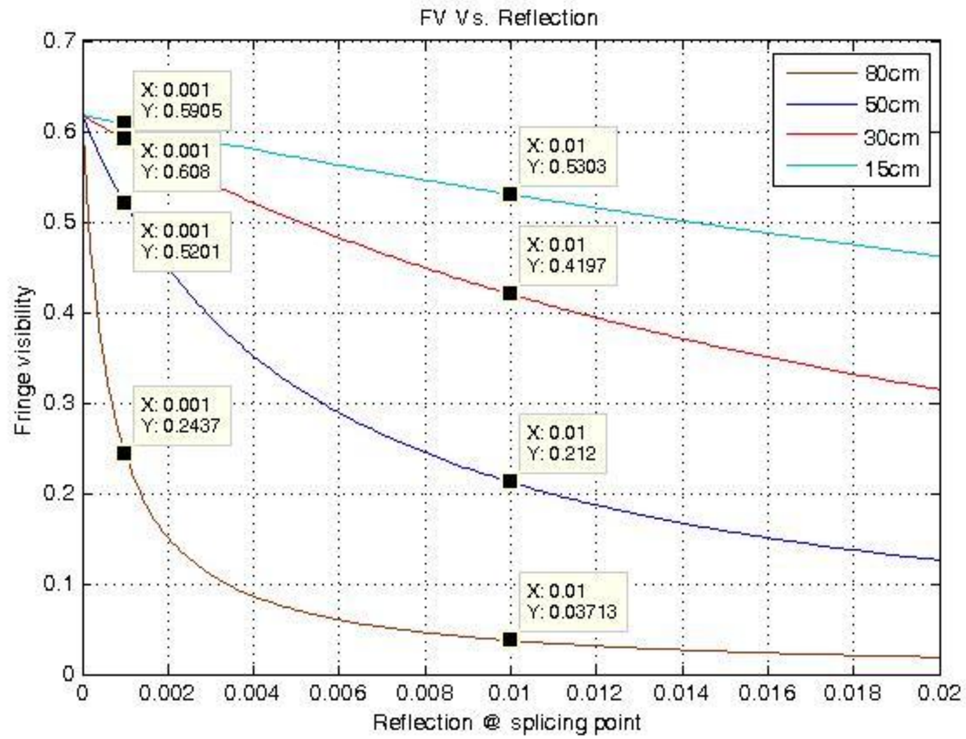

Figure 4.2-6 Simulation of Fringe Visibility versus Reflection at Splicing Point

Experiments were also done to verify the simulation result. Fringe visibilities are measured with the same sensor head but different angled spliced sapphire fibers. The results are listed in Table 4.2-2 and illustrated in Figure 4.2-7.

Table 4.2-2 Fringe Visibility versus Angled Splicing Result

Polished angle	0°	10°	15°	25°	35°
Average	0.048267	0.053583	0.047333	0.036583	0.025333
Standard Deviation	0.002405	0.001645	0.001891	0.003075	0.001579

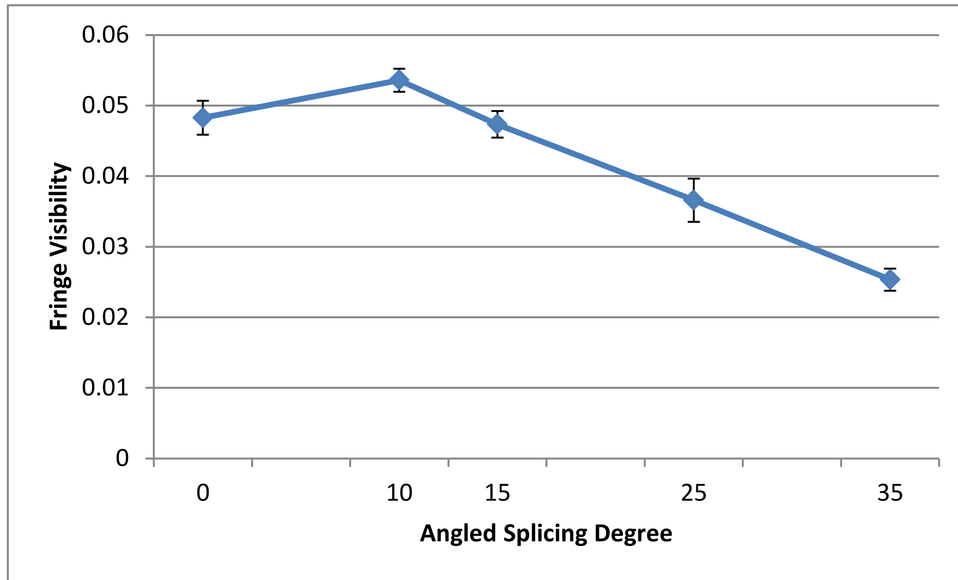

Figure 4.2-7 Fringe Visibility versus Angled Splicing Result

The fringe visibility result seems to disagree with the reflection result in Figure 4.2-4, where 15° splicing appears to have lower reflection than 10° splicing. One explanation for such phenomenon is that as the polishing angle of sapphire fiber increases, light of higher order mode is more likely to be coupled into sapphire fiber, which would suffer greater loss than lower order modes. Therefore the fringe visibility is a tradeoff between reflection and loss, and 10° angled splicing appears to be the best result.

4.3 Sensor Link Assembly

From the previous sections we are able to determine the length of sapphire fiber, which is $50cm$ and the loss is about 15.2dB. Besides, the configuration for silica-to-sapphire splicing is decided, which is 10° angled polishing and splicing (Figure 4.3-1).

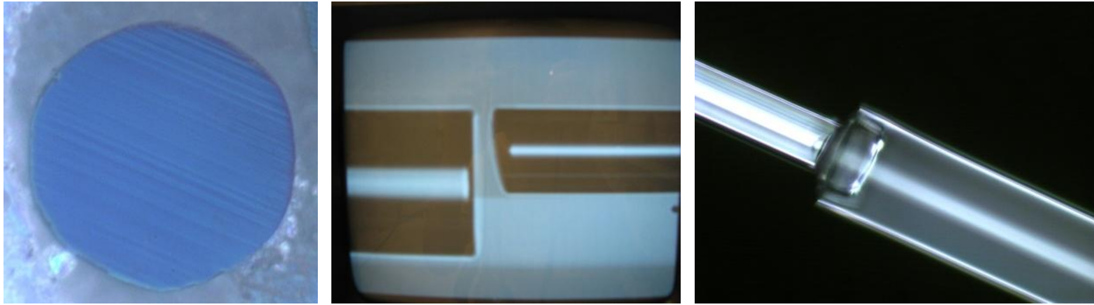

Figure 4.3-1 10° Angled Polishing and Splicing
left: angled polished sapphire fiber, middle: ready to splice fibers, right: spliced fiber

A detailed design based on Figure 2.4-4 has been proposed for real sensor link assembly (Figure 4.3-2). The sapphire fiber is protected by a flexible sapphire tube, with outer diameter around $800\mu m$. The sapphire tube and sensor head are joined together by another piece of alumina tube from which we made the outer tube of sensor head. Additional silica tube with $\approx 200\mu m$ outer diameter is used to protect the silica-to-sapphire splicing point. And the 100/140 multimode fiber is spliced with gold coated fiber because the normal plastic coating for silica fiber can not survive at high temperature (the estimated temperature at splicing point is at least 300°C).

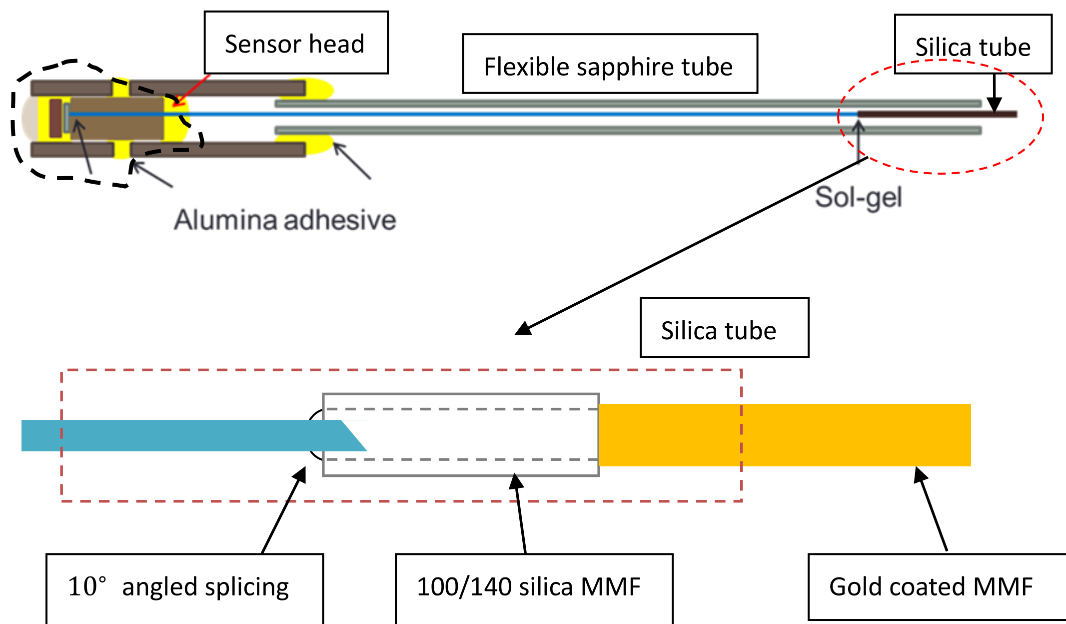

Figure 4.3-2 Sensor Link Assembly – detailed

So far, all the components at extreme high temperature area are alumina and sapphire based, rest of the components at lower temperature area are silica based. Additionally, all the conjunctions at high temperature area are bonded by alumina adhesive. Such configuration is for the consistency of material, reducing the risk of breaking the assembly by mismatching in thermal expansion.

During the whole assembly process, the spectrum was monitored by the interrogation system, which appeared to be very unstable when applying adhesive to the sensor link. Since any small movement of sapphire fiber could result entirely different optical path, and therefore generate a different spectrum. In order to solve such problem, the assembly procedure is broken into two steps.

- Firstly the sapphire fiber and sensor head are glued together using alumina adhesive. And the adhesive is cured by furnace immediately afterwards to stabilize the sapphire fiber within the sensor head.
- After the curing, the rest of sensor link is assembled without concern of sapphire fiber movement. And the rest conjunctions with alumina adhesive can be cured at the same time.

Figure 4.3-3 shows the setup for sensor link assembly. The sensor link was baked in the furnace for the curing procedure, and was inserted in a glass tube to prevent the sensor head from hanging.

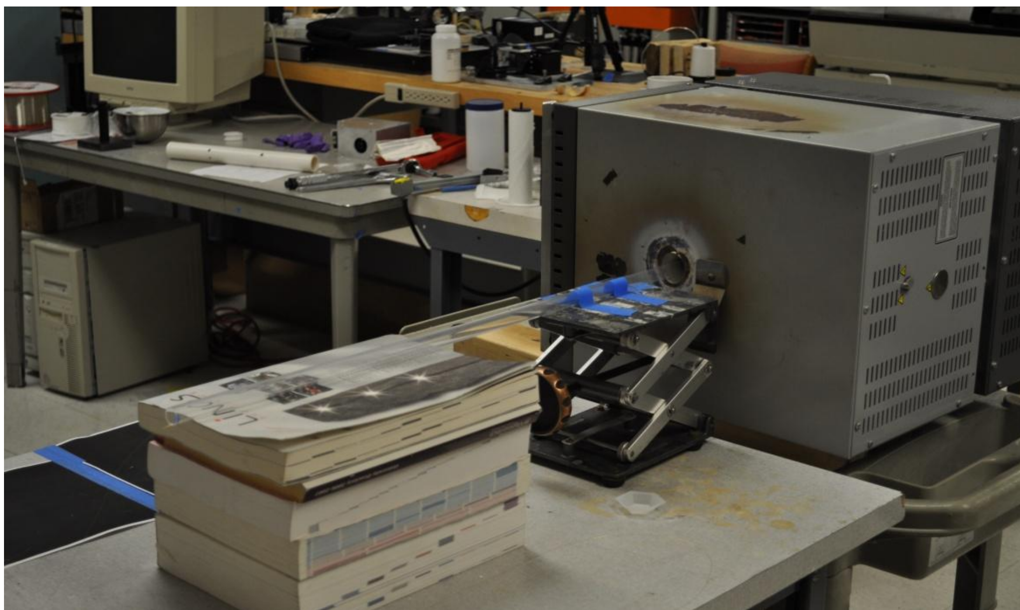

Figure 4.3-3 Sensor Link Assembly Setup

4.4 Signal Processing and Temperature Calibration

As we mentioned previously in Chapter 2, the goal of signal processing is to demodulate the optical path distance (OPD) from the spectrum of light intensity $I(\lambda)$. The typical spectrum we get from the spectrometer is described by Equation 2-4, and can be simplified as:

$$I(\lambda) = AI_0(\lambda) + BI_0(\lambda)\cos\left(\frac{2\pi \times OPD}{\lambda} + \phi\right) + u(\lambda) \tag{4-7}$$

where A, B and ϕ are characterized by the sensor link and assumed to be wavelength independent. The measured spectrum includes a "DC" background components $AI_0(\lambda)$, an amplitude modulated (AM) OPD signal $BI_0(\lambda)\cos\left(\frac{2\pi \times OPD}{\lambda} + \phi\right)$ and white noise $u(\lambda)$.

One straight forward approach is to divide Equation (4-7) by the incident light source spectrum $I_0(\lambda)$, to have a normalized light intensity, which becomes a simpler problem to estimate the frequency of a sinusoid function.

$$I_{normal}(\lambda) = A + B\cos\left(\frac{2\pi \times OPD}{\lambda} + \phi\right) + u'(\lambda) \tag{4-8}$$

The difficulty of this approach is the source spectrum needs to be updating in real time since the sensor would experience temperature changes, which would also affect the $I_0(\lambda)$.

Previous work by Fabin Shen[28] introduced a signal processing method for white light based interferometers. The idea of Shen's method is to transform the AM term into the total phase, rather than demodulating the AM signal directly. Change Equation 4-7 into wavenumber domain:

$$I(k) = I_0(k)\exp[j(kL + \phi)] \tag{4-9}$$

The OPD is defined as L, and wavenumber $k = \frac{1}{\lambda}$. The AM signal can be obtained through a band pass filter to eliminate the "DC" components. After the filtering, the analytical signal can be written as

$$x_n = A_n \exp[j(k_n L + \phi)] + u'_n = A_n \exp[j(k_s L n) + k_0 L + \phi] + u'_n \tag{4-10}$$

A_n is the amplitude after filtering, and u'_n is the filtered white noise. k_n refers to

uniform distributed wavenumbers, starting from k_0, with step k_s.

A frequency estimation[29] based on linear regression of the instantaneous signal phase was used to estimate $k_n L$. The total phase of x_n can be estimate as

$$\phi_n = \tan^{-1}\left[\frac{Im(x_n)}{Re(x_n)}\right] + 2m\pi = k_n L + \phi + u_n'' \quad (4\text{-}11)$$

u_n'' comes from the white noise, and $n = [1, \dots, N]$ represent the length of k_n. L and ϕ can be estimated by linear regression which minimize the square error

$$S = \sum\left[\phi_n - k_n \hat{L} - \hat{\phi}\right]^2 \quad (4\text{-}12)$$

The solution to 4-12 is

$$\begin{bmatrix} \hat{L} \\ \hat{\phi} \end{bmatrix} = (A^T A)^{-1} A^T \Phi \quad (4\text{-}13)$$

where

$$A = \begin{bmatrix} k_1 & k_2 & \cdots & k_N \\ 1 & 1 & \cdots & 1 \end{bmatrix}^T$$

$$\Phi = [\phi_1 \quad \phi_2 \quad \dots \phi_N]^T$$

However, estimated $\hat{L}$ may not have very high accuracy, especially when the fringe visibility is low. In practice, the phase term ϕ in Equation 4-9 would remain constant during the calibration. Therefore we can use Equation 4-13 to calculate ϕ and average the data and set it as calibration for L calculation. Such OPD estimation is more accurate from directly calculated OPD from Equation 4-12.

The sensor links we made were calibrated using a similar setup with Figure 4.3-3. In addition to the thermal measurement by furnace itself, a thermal couple was put as the adjacent location in the furnace with the sensor head, in order to obtain more accurate temperature data. The calibration was done by cycling temperature between room temperature and 1200℃, therefore the glass tube can no longer be used, or it would melt.

The spectrum data was taken at 50℃ during ramping up and 100℃ during ramping down. The data was then interpreted by Shen's algorithm for the OPD data. Figure4.4-1 and 4.4-2 show calibration results for two cycles and the relationship between temperature and OPD is close to linear, with slope $0.631℃/nm$.

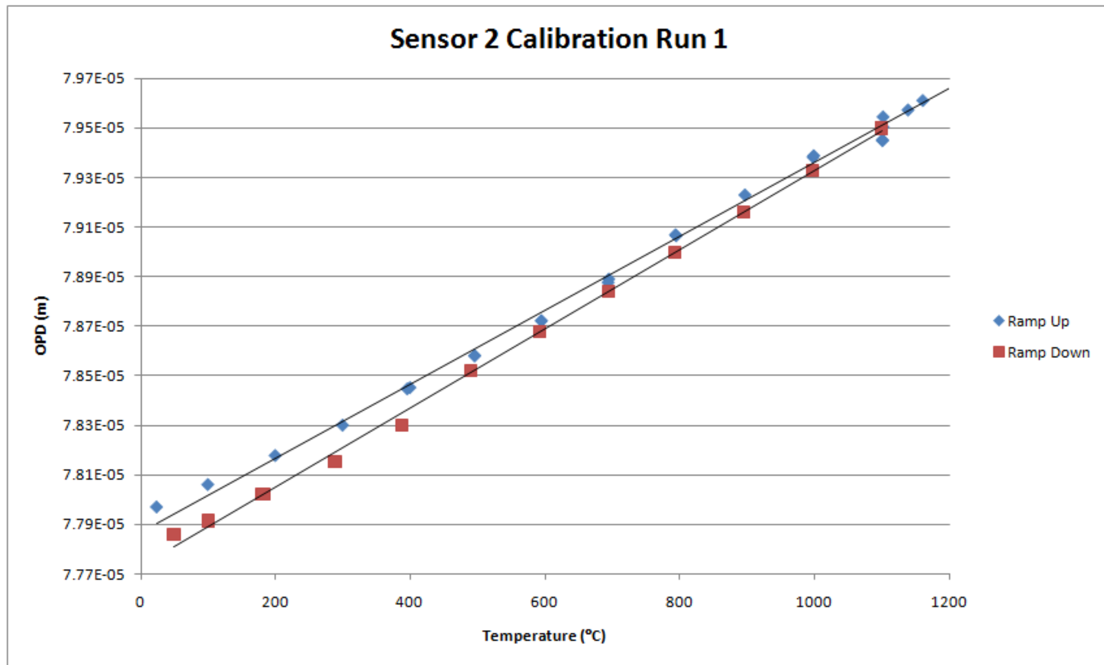

Figure 4.4-1 Sensor 2 calibration Result – Run 1

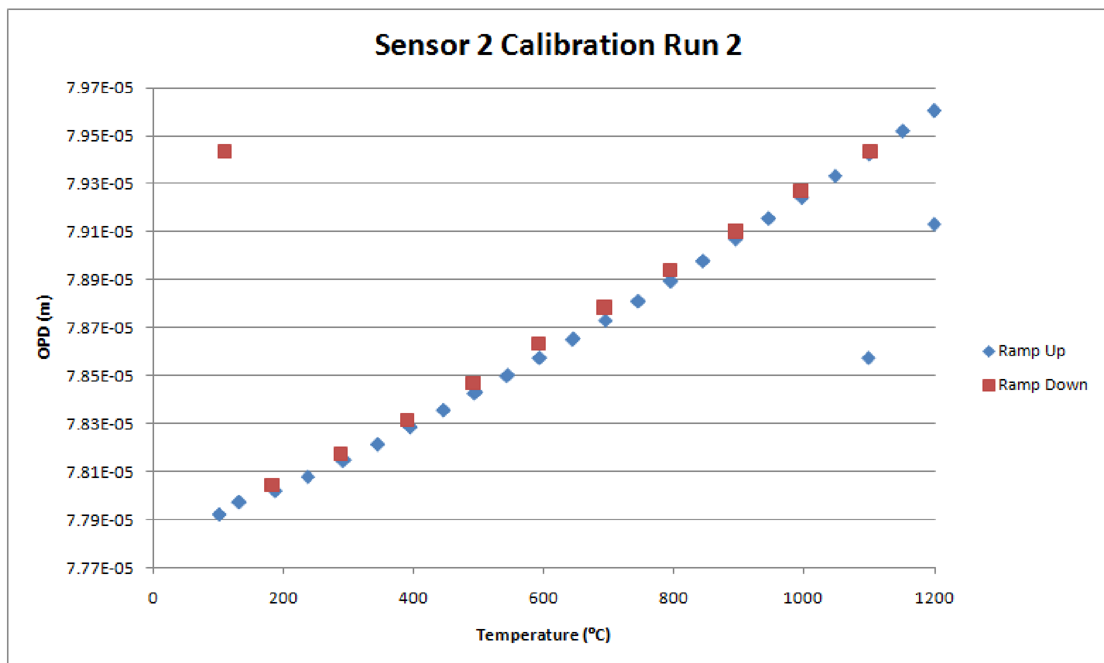

Figure 4.4-2 Sensor 2 calibration Result – Run 2

Chapter 5.

Conclusions

5.1 Conclusions

Our research has demonstrated an improved design of sapphire-based higher temperature fiber optic sensors. Besides their minimized size (Figure 5.1-1), the sensors have shown accurate response during temperature calibration, with high resolution and strong robustness.

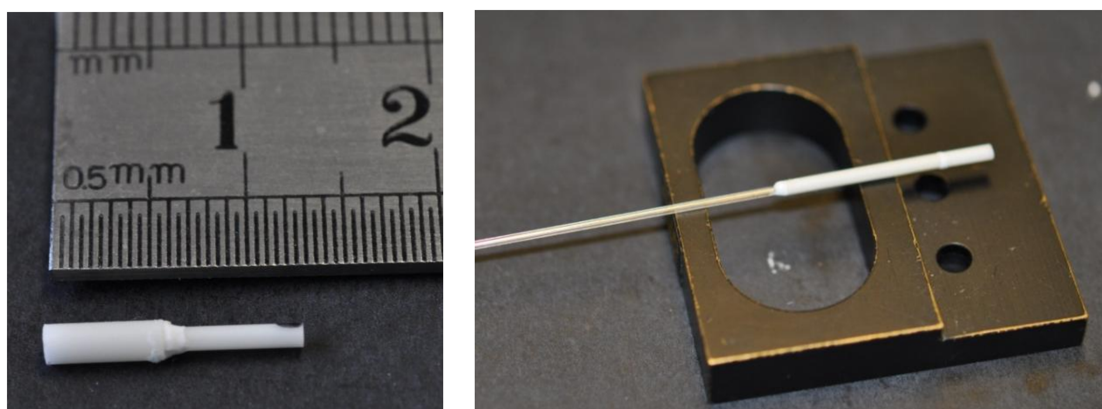

Figure 5.1-1 Sensor Dimensions
left: sensor head dimensions, right: sensor head after assembly

In summary, the sensing component is an EFPI sensor with sapphire wafer of $20\mu m \sim 30\mu m$ as the F-P cavity. Light propagates through a silica-sapphire combined fiber link, reflected by the sensor head and collected by a white light based interferometer interrogation system. The sensors were proven to be functional after high temperature annealing up to 1600℃, and have shown linear sensing response during $20 \sim 1200$℃ temperature calibration.

5.2 Suggestions for Future Work

Although the sensor of current design has illustrated excellent sensing ability within a large dynamic range, much work can be done to improve the design.

5.2.1 Sensor Head Design

Wafer based sensor head is able to achieve very high fringe visibility with thin wafers down to $20\mu m$ and less. But the assembly procedure usually degrade the fringe visibility by at least $2\sim 3dB$. A thin film based sensor design can largely reduce the loss during assembly, and also provides even thinner F-P cavity. Previously thin film based temperature sensor has been demonstrated on silica fiber[30]. Adopting similar sensor scheme could largely improve the fringe visibility and reduce the difficulty of sensor head assembly.

5.2.2 Silica-to-Sapphire Splicing

The angled polishing and splicing technique we developed for this sensor link design is able to reduce the loss and degradation of fringe visibility at silica-to-sapphire fiber splicing. But the improvement is limited by the drawback effect of greater loss due to the generation of higher order modes.

Figure 4.2-6 shows a promising improvement in fringe visibility when eliminating or reducing the reflection at splicing point. An intermediate thin film can be used as anti-reflection coating (Figure 5.2-1).

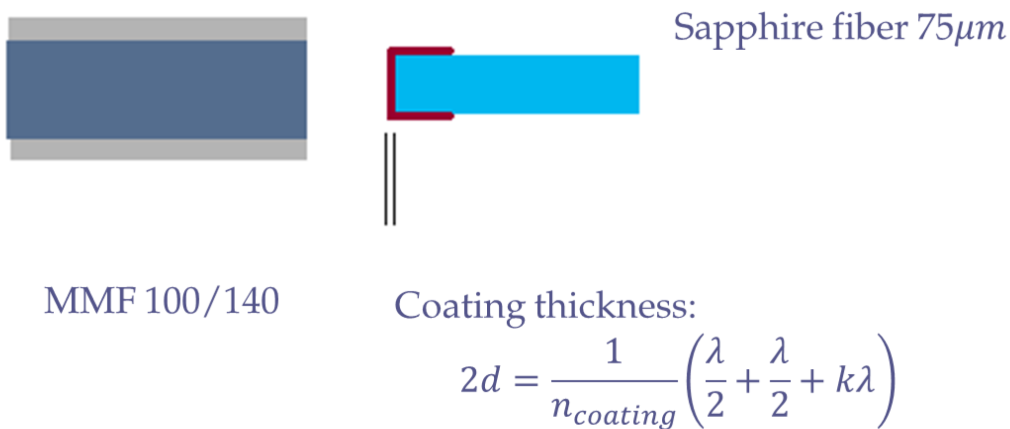

Figure 5.2-1 Thin Film Anti-reflection Coating for Splicing Point

Coating material like Ta_2O_5 has refraction index in the middle of silica and sapphire material, and the thermal expansion coefficient is close to these two materials as well. It could provide a possible candidate for the anti-reflection coating material.

Reference

[1] Narinder Singh Kapany, a series of papers in Scientific American, as well as the book: *Fiber Optics: Principles and Applications*, 1967

[2] A. J. Rogers, *Optical methods for measurement of voltage and current at high voltage*, Optics & Laser Technology, 1977

[3] Yizheng Zhu, Anbo Wang, *Miniature fiber-optic pressure sensor,* Photonics Technology Leters, IEEE, 2005

[4] G. Pickrell, W. Peng, and A. Wang, *Random-hole optical fiber evanescent-wave gas sensing,* Optics Letters, 2004

[5] Grattan, K. and B. Meggitt, *Optical fiber sensor technology: devices and technology*, 1998

[6] Quick et al, *Fiber optic temperature sensor*, United States Patent

[7] Chung E. Lee and Henry F. Taylor, *Fiber-optic Fabry-Perot Temperature Sensor Using a Low-Coherence Light Source*, Journal of Lightwave Technology, 1991

[8] Z. Y. Zhang et al, *Spectral characteristics and effects of heat treatment on intrinsic Nd-doped fiber thermometer probes*, Rev. Sci. Instrum, 1998

[9] Z. Y. Zhang et al, *Thulium-doped intrinsic fiber optic sensor for high temperature measurements (>1100 °C)*, Rev. Sci. Instrum, 1998

[10] Tyson L. Lowder et al, *High-Temperature Sensing Using Surface Relief Fiber Bragg Gratings,* IEEE Photonics Technology Letters, 2005

[11] A. Wang, S. Gollapudi, K. A. Murphey, R. G. May, and R. O. Claus, *Sapphire-fiber-based intrinsic Fabry-Perot interferometer,* Optics. Letters, 1992

[12] R. R. Dils, *High-temperature optical fiber thermometer*, J. Applied Physics, 1983

[13] R. R. Dils, J. Geist, and M. L. Reilly, *Measurement of the silver freezing point with an optical fiber thermometer: Proof of concept,* J. Applied Physics, 1986

[14] J. L. Kenndey, and N. Djeu, *Operation of Yb:YAG fiber-optic temperature sensor up to 1600*°C, Sensors Actuators, 2002

[15] A. Wang et al, *Advances in sapphire-fiber-based intrinsic interferometric sensors,* Opt Let. 1992

[16] A. Wang et al, *Sapphire optical fiber-based interferometer for high temperature environmental applications*, Smart Materials and Structures, 1995

[17] Yizheng Zhu, *Miniature Fiber-Optic Sensors for High-Temperature Harsh Environments,* dissertation for Doctor in Electrical Engineering, Virginia Tech. 2007

[18] http://www.fossil.energy.gov/programs/powersystems/gasification/index.html

[19] http://en.wikipedia.org/wiki/Coal_gasification

[20] Murphy et al, *Quadrature phase-shifted, extrinsic Fabry-Perot optical fiber sensors*, Optics Letters, 1991

[21] Cheng Ma et al, *Intrinsic Fabry-Pȳrot interferometric (IFPI) fiber pressure sensor,* Proc. SPIE 2010

[22] Cheng Ma et al, *Decoding the spectra of low-finesse extrinsic type optical fiber Fabry-Perot interferometers*, Optics Express (to be submitted), 2011

[23] R. E. Wagner, and C. R. Sandahl, *Interference effects in optical fiber connections*, Applied Optics, 1982

[24] F. Perennes et al, *Analysis of a low-finesse Fabry-Perot sensing interferometer illuminated by a multimode optical fiber*, Applied Optics, 1999

[25] http://www.oceanoptics.com/Products/usb2000.asp

[26] http://www.valleydesign.com/

[27] Georgi Ivanov, Fabry-Pyrot Sapphire Temperature Sensor for Use in Coal Gasification, thesis for Master in Electrical Engineering, Virginia Tech. 2011

[28] Fabin Shen and Anbo Wang, *Frequency-estimation-based signal-processing algorithm for white-light optical fiber Fabry–Perot interferometers*, Applied Optics, 2005

[29] S. A. Tretter, *Estimating the frequency of a noisy sinusoid by linear regression*, IEEE Trans. Inf.

Theory, 1985

[30] J Chen et al, *Simple thin-film fiber optic temperature sensor based on Fabry-Perot interference*, Optical Engineering, 2010